Effects of Eddy Vorticity Forcing on the Mean State of the Kuroshio Extension

ANDREW S. DELMAN, JULIE L. MCCLEAN, JANET SPRINTALL,
LYNNE D. TALLEY, AND ELENA YULAEVA

Scripps Institution of Oceanography, University of California, San Diego, La Jolla, California

STEVEN R. JAYNE

Woods Hole Oceanographic Institution, Woods Hole, Massachusetts

(Manuscript received 27 November 2013, in final form 18 February 2015)

ABSTRACT

Eddy–mean flow interactions along the Kuroshio Extension (KE) jet are investigated using a vorticity budget of a high-resolution ocean model simulation, averaged over a 13-yr period. The simulation explicitly resolves mesoscale eddies in the KE and is forced with air–sea fluxes representing the years 1995–2007. A mean-eddy decomposition in a jet-following coordinate system removes the variability of the jet path from the eddy components of velocity; thus, eddy kinetic energy in the jet reference frame is substantially lower than in geographic coordinates and exhibits a cross-jet asymmetry that is consistent with the baroclinic instability criterion of the long-term mean field. The vorticity budget is computed in both geographic (i.e., Eulerian) and jet reference frames; the jet frame budget reveals several patterns of eddy forcing that are largely attributed to varicose modes of variability. Eddies tend to diffuse the relative vorticity minima/maxima that flank the jet, removing momentum from the fast-moving jet core and reinforcing the quasi-permanent meridional meanders in the mean jet. A pattern associated with the vertical stretching of relative vorticity in eddies indicates a deceleration (acceleration) of the jet coincident with northward (southward) quasi-permanent meanders. Eddy relative vorticity advection outside of the eastward jet core is balanced mostly by vertical stretching of the mean flow, which through baroclinic adjustment helps to drive the flanking recirculation gyres. The jet frame vorticity budget presents a well-defined picture of eddy activity, illustrating along-jet variations in eddy–mean flow interaction that may have implications for the jet's dynamics and cross-frontal tracer fluxes.

1. Introduction

The western boundary current of the North Pacific separates from the coast of Japan as a fast, energetic narrow jet known as the Kuroshio Extension (KE). The KE jet path is variable and often highly meandering as it flows eastward, crossing ridges of relatively shallow bathymetry at approximately 140° and 160°E (Fig. 1). Part of this meandering pattern is quasi stationary, with mean crests in the jet path around 143°–144° and 150°E and a trough near 146°E; this pattern is attributed to lee waves downstream of the Izu–Ogasawara Ridge (Mizuno and White 1983). The jet is flanked by recirculation gyres to the south (e.g., Niiler et al. 2003) and north (Qiu et al. 2008; Jayne et al. 2009), though the subsurface northern gyres are weaker and generally linked to troughs in the quasi-stationary meanders (Jayne et al. 2009; Tracey et al. 2012).

The KE is also associated with the highest levels of mesoscale eddy activity in the North Pacific (Qiu and Chen 2010). In energetic western boundary current extensions, mesoscale eddies are thought to play an important role in cross-jet transport of tracers such as heat (e.g., Wunsch 1999; Qiu and Chen 2005; Bishop et al. 2013) and momentum (e.g., Hall 1991; Adamec 1998; Greatbatch et al. 2010; Waterman et al. 2011). Mesoscale eddy activity in the KE region is complex and takes a variety of forms. Meanders in the KE jet are steepened, likely from baroclinic instability [as shown by Shay et al. (1995) in the Gulf Stream] driven by vertical coupling between the surface meanders and deep pressure/current anomalies (Bishop and Bryan 2013). These meanders then frequently pinch off the jet as rings that essentially extend to the bottom of the water column. Moreover,

Corresponding author address: Andrew S. Delman, Scripps Institution of Oceanography, University of California, San Diego, 9500 Gilman Dr., MC 0208, La Jolla, CA 92093.
E-mail: adelman@ucsd.edu

DOI: 10.1175/JPO-D-13-0259.1

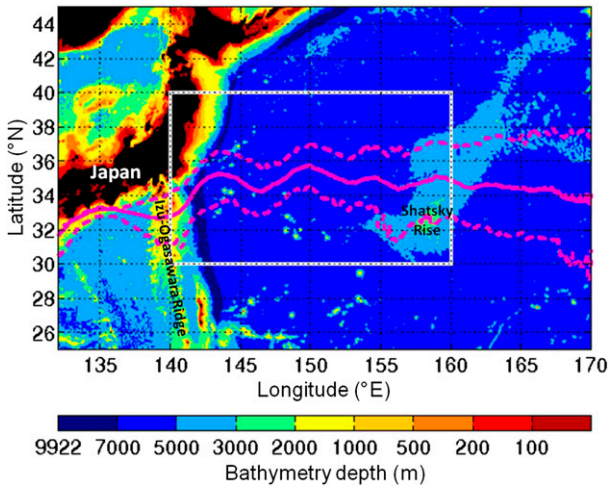

FIG. 1. Bathymetry in the Kuroshio Extension region. The magenta lines indicate the mean (solid) and 10th/90th percentile (dashed) jet axis positions computed from POP for 1995–2007. The jet axis position for each 5-day period is defined as the 5-day mean SSH contour associated with the steepest gradients of SSH in the study region (white rectangle). The jet axis position is then extended outside the study region along the same SSH contour. For more details on how the jet axis is defined, see section 3a.

deep topographically controlled eddies (whether generated from the downstream jet or elsewhere) propagate generally southwestward along f/H contours, with length scales (half wavelengths) of 175–350 km and periods of 30–60 days (Greene et al. 2012). These eddies may produce changes in the path and cross-frontal structure of the KE jet (Tracey et al. 2012; Greene et al. 2012) and drive large divergent heat fluxes across the jet (Bishop 2013). Smaller perturbations (with approximately 100–200-km length scales and 4–60-day periods) in the KE jet, often called frontal waves, propagate downstream along the jet and may interact with the topographically controlled eddies to amplify or damp their influence, depending on their relative phasing (Tracey et al. 2012).

Because of the highly variable path of the KE jet, time averages of velocity and state variables in the KE region often smooth or obscure the true cross-jet structure; this problem has been successfully dealt with in the KE by transforming these fields into a stream coordinate reference frame relative to the jet (e.g., Howe et al. 2009; Waterman et al. 2011). Waterman et al. (2011) used this approach to estimate the eddy–mean flow interaction from observations, suggesting that eddies were helping to drive the mean jet and recirculations near the eddy kinetic energy (EKE) maximum at 146°E. However, in situ observations of eddy momentum fluxes have generally been limited to either a small number of transects or an array spanning 5°–6° longitude [i.e., the Kuroshio Extension System Study (KESS) array; Donohue et al. 2008] and are also constrained to time periods ranging from synoptic snapshots (Howe et al. 2009) to sporadic 2-yr field campaigns (Waterman et al. 2011).

The extension of spatial and temporal coverage offered by ocean general circulation models (OGCMs) provides an opportunity to study the along-jet and cross-jet variations in eddy forcing. Eddy forcing likely varies with longitude along the KE jet axis, influenced by bathymetric ridges underlying the jet (Fig. 1) as well as position relative to the maximum in EKE at 146°E. Quasigeostrophic models of idealized western boundary current extensions (e.g., Jayne et al. 1996; Waterman and Jayne 2011; Waterman and Hoskins 2013) in particular suggest that the sign of eddy forcing may vary in the along-jet direction near the eastward jet's EKE maximum. Previous studies using OGCMs (Qiu et al. 2008; Taguchi et al. 2010) have considered the effect of eddy potential vorticity (PV) fluxes on the KE northern recirculation gyre at a middepth level ($\sim 27.6\sigma_\theta$). Qiu et al. (2008) determined that the eddy PV flux convergence largely reinforces the mean circulation at middepths, helping to drive the northern recirculation gyre. Additional insights can be gained from an OGCM regarding the long-term mean effects of eddy forcing in the near-surface ocean.

In this study, we examine how transient mesoscale eddies redistribute vorticity along the near-surface KE jet. The central objective of this work is to clarify the long-term effect of eddies on jet velocities and cross-frontal gradients as well as on the recirculation gyres flanking the jet. An eddying ocean simulation, run using the Parallel Ocean Program (POP), with 13 yr of simulated KE variability is used to construct a vorticity budget in the vicinity of the narrow jet. In particular, our analysis employs a jet reference frame to preserve the jet's sharp gradients and so clarify the forcing from eddy vorticity fluxes on the mean jet, and how this forcing varies with longitude as well as across the jet. The paper is organized as follows: Section 2 describes the multiyear ocean model simulation. Section 3 details the stream coordinate or jet reference frame used in our analysis, with a comparison of the jet characteristics and eddy activity as viewed in geographic (i.e., Eulerian) and jet-following reference frames. Section 4 considers the depth-averaged vorticity budget in the geographic and jet reference frame, isolating the eddy terms and detailing their contribution to the budget. Section 5 discusses patterns of eddy forcing that are identified from the jet frame vorticity budget results. In section 6, a brief study of the long-term mean baroclinic instability criteria is presented to offer some context for the results of the jet frame analyses; section 7 offers a short summary of our findings and some conclusions.

2. Model description

POP is an ocean general circulation model that solves the three-dimensional primitive equations for ocean dynamics (Smith and Gent 2002; Smith et al. 2010). The model was run in the global domain, with nominal 0.1° horizontal resolution (~8 km in the Kuroshio Extension region) on a tripole grid, with two northern poles in Canada and Russia. The grid was configured with 42 vertical levels and ~10-m vertical spacing near the surface and utilizes the *K*-profile parameterization (KPP; Large et al. 1994) scheme for finescale (~10 m) vertical mixing. Biharmonic viscosity and diffusivity are used, with equatorial values of $\nu_0 = -9 \times 10^9\,\mathrm{m^4\,s^{-1}}$ and $\kappa_0 = -3 \times 10^9\,\mathrm{m^4\,s^{-1}}$ that decrease as a function of the grid spacing cubed at higher latitudes so that the viscous term can balance the nonlinear advection terms (Maltrud et al. 1998). Modest surface salinity restoring was incorporated to limit drift, as were partial bottom cells to improve the representation of flow over bottom topography, which is important for representing the interactions with the ridges that underlie the KE.

The model run was initialized from year 30 of an existing POP run that was configured on the same tripole grid [for more details see Maltrud et al. (2010)], forced with Coordinated Ocean Research Experiments (CORE) normal-year surface fluxes representing a repeating annual cycle in the atmosphere (Large and Yeager 2004), with added synoptic-scale variability averaged to monthly intervals. Our model run was then forced with the CORE version 2 (CORE2) surface fluxes representing synoptically and interannually varying atmospheric conditions during the years 1990–2007 (Large and Yeager 2009). Daily mean state variables, surface fluxes, and advective fluxes were archived from 1995 to 2007 (postadjustment to high-frequency atmospheric forcing) for most of the North Pacific, including horizontal fluxes of momentum Uu, Uv, Vu, and Vv. The effective flux velocities U and V are weighted (six point) horizontal averages of u and v, respectively, defined such that both momentum and kinetic energy are conserved by advection on an Arakawa B grid [for details of the calculation see Smith and Gent (2002) and Smith et al. (2010)]. The archived horizontal momentum fluxes are particularly useful for quantifying the role of higher-frequency mesoscale variability in the vorticity balance throughout the KE region.

3. The jet reference frame

a. *Defining a jet reference frame*

Daily averages of the KE flow (e.g., Figs. 2a,b) typically depict much sharper sea surface height (SSH) gradients across the jet than are evident from geographic means over longer time periods (Figs. 2c,d). This discrepancy results from large, short-period fluctuations in the KE jet path (e.g., Fig. 2 in Qiu and Chen 2010), associated with propagating eddies and frontal waves. Consequently, the path of the jet varies meridionally by over 300 km in some areas (Fig. 1)—much more than the typical KE jet width of 100–200 km (Figs. 2a,b; Fig. 7 of Waterman et al. 2011).

A more useful method of averaging KE jet features over long time periods (e.g., Bingham 1992; Waterman et al. 2011) is to transform data into a jet reference frame. Bingham (1992) used a jet-following coordinate frame with two horizontal dimensions: the x coordinate was the longitude of the nearest point on the jet axis, and the y coordinate was the distance from the jet axis. Our approach differs slightly in that we retain the longitude of the data point itself as the x coordinate so that the effects of bathymetry are as faithfully represented in long-term means as possible. Fields in the POP model are averaged in bins that correspond to the longitude of the grid points and their distance to the closest point on the jet axis.

To transform into the jet reference frame, it is first necessary to come up with a consistent objective method for identifying the jet axis (the zero y coordinate in the jet reference frame). For the upper ocean, a fixed contour of SSH or temperature (Jayne et al. 2009; Waterman et al. 2011) or identified maxima in velocity magnitude (Howe et al. 2009) may be used to define the jet axis. Other criteria used to define the jet axis may be based on velocity shear (as described in Meinen and Luther 2003) or gradients of SSH, temperature, or other properties that vary across the front. To define a jet path that follows the along-stream direction of the flow as closely as possible, we considered jet definitions using fixed contours of SSH (50 cm; Jayne et al. 2009) and temperature (12°C at 350-m depth; Waterman et al. 2011). In addition, we implemented a "steepest (SSH/temperature) gradient" method that identifies the SSH or temperature contours at each time interval collocated with the steepest gradients of SSH and 350-m temperature in a geographic range (30°–40°N, 140°–160°E) that corresponds to the KE (Fig. 1). Of all these methods, the SSH steepest gradient method most consistently tracked the maximum velocity jet core in POP during the 13-yr study period; hence, our study employs this technique as described below.

To define the jet axis for each time period that will serve as the zero coordinate in the cross-jet direction, SSH from the model output was first averaged in 5-day periods. The 5-day time average was chosen to minimize the rapid oscillations of the jet path that can occur as

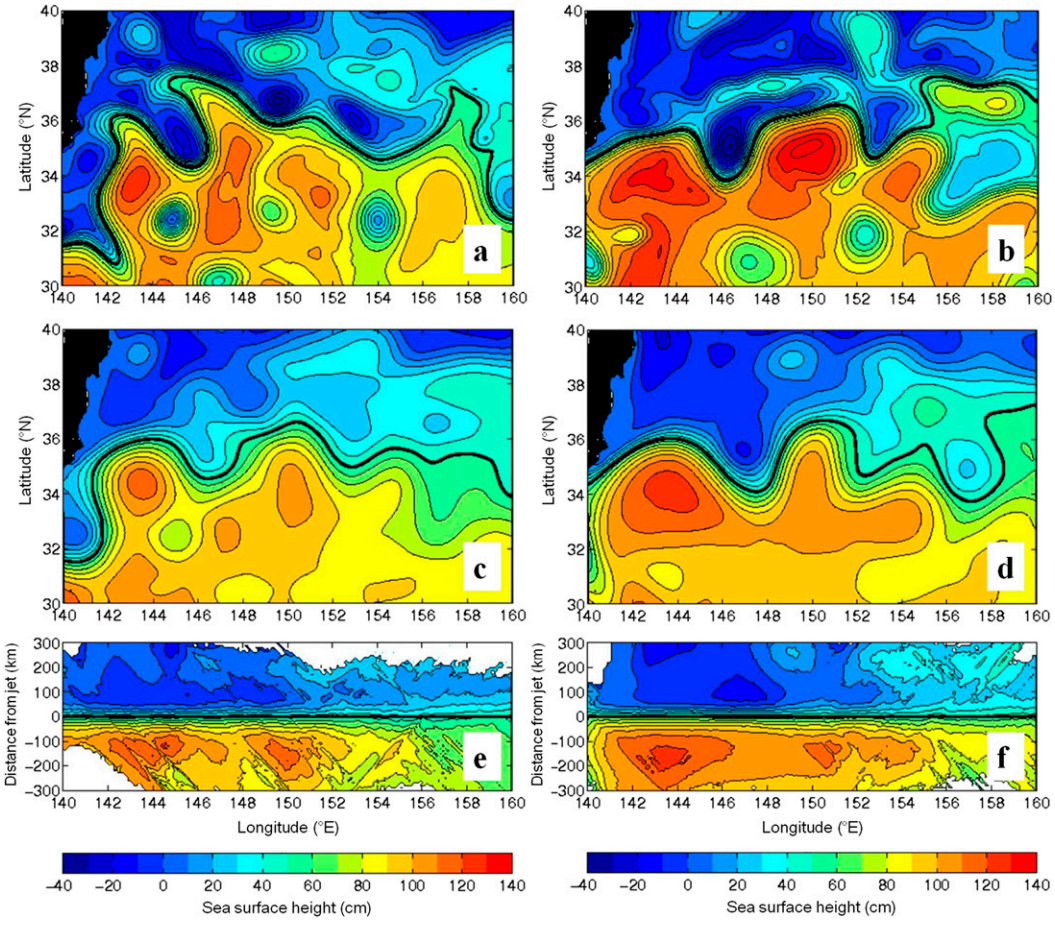

FIG. 2. POP SSH daily snapshots on (a) 22 Jun 1997 and (b) 17 Jul 1998, with the thick black line indicating the 50-cm contour. POP SSH annual geographic means for (c) 1997 and (d) 1998, with the 50-cm contour indicated as in (a) and (b). POP SSH annual jet frame means for (e) 1997 and (f) 1998, as computed using the steepest gradient SSH method; the thick black line indicates the jet axis. The color scale is the same for (a)–(f) and is indicated by the color bars below (e) and (f). The contour interval for all panels is 10 cm.

closed SSH contours (representing rings) pinch off from or reattach to the jet axis contour, while still averaging at a short enough time scale to follow the variations in the jet path due to most mesoscale features.

Next, the value of the jet axis SSH contour was computed for each 5-day period. Zonal and meridional derivatives of the 5-day mean SSH were computed in the model native grid, with the SSH interpolated before the derivatives were taken so that the zonal and meridional derivatives were computed on the same grid as the SSH values they are derived from. From the zonal and meridional SSH derivatives, the magnitude of the SSH gradient $|\nabla(\mathrm{SSH})|$ was obtained. Then the top 5% of $|\nabla(\mathrm{SSH})|$ values were binned according to the values of SSH at the same locations, creating a probability distribution function (PDF). A Gaussian smoothing function was applied to the PDF to reduce the sensitivity of the maximum in the function to isolated peaks (such as might be associated with rings) and sampling biases that might result from the position of SSH contours relative to the model grid. The value of SSH associated with the maximum in the Gaussian-smoothed PDF was the SSH contour that defined the jet axis for that 5-day period. This method allows the contour to vary with seasonal and interannual changes in steric height, rather than using the same SSH contour to represent the jet axis at all time periods.

As a final filter, the length of the jet axis SSH contour was computed for each 5-day time period; in our case, this was done for a larger domain (135°–170°E) to allow for some continuity of the defined jet axis with regions just outside of the study domain 140°–160°E. The SSH contours that had a length below a certain threshold (80% of the zonal distance between 135° and 170°E) were considered unreliable, as these contours likely encompass rings rather than the true KE jet axis;

this can occur during instances when a large ring has gradients around its edge that are nearly uniformly as steep or steeper than those at the true KE jet axis. In our analysis, the unreliable SSH contours constituted about 5% of all the jet axis contours, and the 5-day time periods corresponding to them were not included in the final averages. The remaining viable jet axes (which account for 95% of the 5-day periods from the 1995–2007 model output) were used in our jet frame analyses.

b. *Jet reference frame binning and time averaging*

Once the jet axes have been defined for each 5-day time period, the model grid points at each time period can be assigned a distance from the nearest point on the jet axis d and a local jet orientation angle θ that is important for averaging vector quantities in the jet frame (for a more detailed description of how d and θ are computed see the appendix, section a). The time average relative to the jet is computed by first binning the model grid points according to their longitude ϕ and values of d. Given a scalar quantity A, the angle bracket notation $\langle A \rangle$ indicates the set of values of A located at grid points in a given bin; for a bin centered at $\phi = \phi_m$ and $d = d_n$, the set $\langle A \rangle|_{(\phi_m, d_n)}$ includes model grid points in the ranges $\phi_m - \Delta\phi/2 \le \phi < \phi_m + \Delta\phi/2$ and $d_n - \Delta d/2 \le d < d_n + \Delta d/2$. The bin sizes $\Delta\phi = 0.1°$ and $\Delta d =$ 10 km were chosen for the purposes of this study to correspond approximately to the spacing between model grid points. Once the values of A are sorted into bins, the jet frame time average of A in a given bin is the mean of all the points in that bin, denoted by $\overline{\langle A \rangle}^j$. To apply the jet frame time average to a vector quantity $\mathbf{u}$, the components of the vector aligned with the local jet frame axes $\mathbf{u}_j = (u_j, v_j)$ must first be computed, requiring a rotation of the vector by the orientation angle θ. This process is described in more detail in the appendix, section b.

c. *Jet characteristics in the geographic and jet reference frames*

Time averages of jet properties such as SSH, currents, and pressure (Jayne et al. 2009; Waterman et al. 2011) are notably different when averaged in geographic and jet reference frames. The near-axis jet frame velocity maximum is more than twice the magnitude of the geographic mean velocity maximum in observations (Waterman et al. 2011), with steeper velocity gradients evident on the flanks of the jet. Here, we consider 0–250-m, depth-averaged properties of the jet that have been time averaged in geographic and jet reference frames. The upper 250 m of the water column encompasses the fastest velocities in the jet axis core as identified from observations (e.g., Howe et al. 2009; Waterman et al. 2011) and POP. Most of the eddy kinetic energy in the region of interest as depicted by POP also occurs in the upper 250 m. Figure 3 shows that the jet frame velocity variance terms at 146°E [the longitude of the observations discussed in Waterman et al. (2011)] decay rapidly and fairly uniformly with depth, indicating that the 0–250-m layer is representative of the upper ocean; hence, we use this layer in subsequent analyses.

As with observations, the cross-jet velocity profile in POP at 146°E is much sharper in the jet frame mean $\overline{\langle \mathbf{u}_j \rangle}^j$ than in the geographic mean $\overline{\mathbf{u}}$ (Fig. 4; compare to Fig. 11a in Waterman et al. 2011). The jet reference frame clearly depicts the high surface velocities ($>1\ \mathrm{m\,s^{-1}}$) that are nearly always present at the jet axis but often obscured in long-term geographic means. All of the eastward flow in the main jet is confined to a band ~200 km wide, with clearly defined (if much slower) westward recirculations on either side of the jet. Likewise, the sharp SSH gradients in the jet reference frame (Figs. 2e,f) are generally contained within a band of ~100 km, as opposed to the more diffuse gradients observed in geographic means (Figs. 2c,d). Both geographic and jet frame, along-jet velocity peaks in POP are similar to or slightly stronger than in observations (Fig. 11a from Waterman et al. 2011).

A different view of the 0–250-m, depth-averaged EKE field also emerges when eddy velocities are computed and averaged in the jet frame versus the geographic frame (Fig. 5). The region of elevated geographic mean EKE $|\overline{\mathbf{u}}|^2$ as observed from altimetry (Fig. 5a) has a similar spatial extent as the elevated geographic EKE region computed from SSH gradients in POP (Fig. 5b), though the EKE magnitudes in POP are somewhat higher. The jet path and EKE from POP is similar to that of a high-resolution (nominal 0.08°) HYCOM simulation (Fig. 2a in Kelly et al. 2007), with elevated EKE tracking the jet path and the crests and troughs of the jet path and stronger EKE signatures occurring at approximately the same longitudes. In POP, the elevated geographic EKE region extends ~200 km to either side of the mean position of the jet (Fig. 5b); its width is coincident with the variation in range of the jet axis itself. The jet frame EKE $\overline{\langle |\mathbf{u}_j|^2 \rangle}^j$ (Fig. 5c) is of noticeably smaller magnitude since the jet frame EKE near the jet axis reflects mostly the variance of the along streamflow (Fig. 3) and excludes the part of geographic EKE due to time-varying jet meanders. The jet frame EKE also exhibits tightly defined extremes near the jet axis; minima are found very close to the jet axis on its southern flank, at longitudes where the mean jet is flowing northward

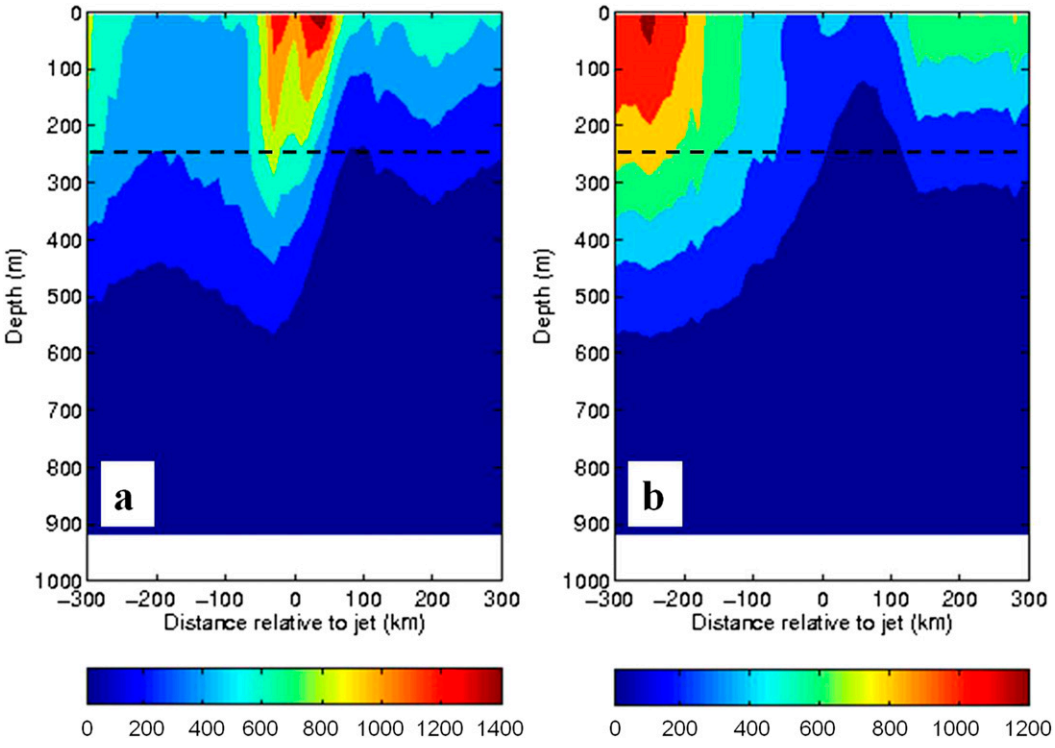

FIG. 3. Eddy variance terms (a) $\overline{\langle u_j' u_j' \rangle}^j$ and (b) $\overline{\langle v_j' v_j' \rangle}^j$ in POP along 146°E, computed in the jet reference frame for 1995–2007. The dashed line indicates 250 m, the base of the upper layer used for depth averaging in our analyses. The color scales are indicated below each figure, with units of $cm^2 s^{-2}$. The contour interval for (a) and (b) is $200\ cm^2 s^{-2}$.

toward a quasi-permanent crest. This suggests that the structure of the south flank of the jet is remarkably stable in some areas, even with large shifts in the jet path's position and orientation. Maxima in the jet frame EKE are found on the north flank of the jet opposite these minima, while separate maxima appear >150 km south and north of the jet, on the other side of the southern and northern recirculation gyres. Section 6 examines the possible effect of the mean jet structure on this cross-jet asymmetry in jet frame EKE.

4. The vorticity budget

Our formulation of the vorticity budget considers a layer of constant depth, with two fixed levels as upper and lower depth bounds. This form is most compatible with a z-level model; that is, one that uses depth as its vertical coordinate. The depth-averaged terms of the budget can then be time averaged either in the geographic or jet reference frame. We first consider the geographic time averages in section 4a to identify any aspects of the KE jet's structure that can be readily understood in an Eulerian coordinate system as well as to provide a comparison with the jet frame results. The jet frame averages are then computed and discussed in sections 4b (full vorticity budget) and 4c (eddy forcing).

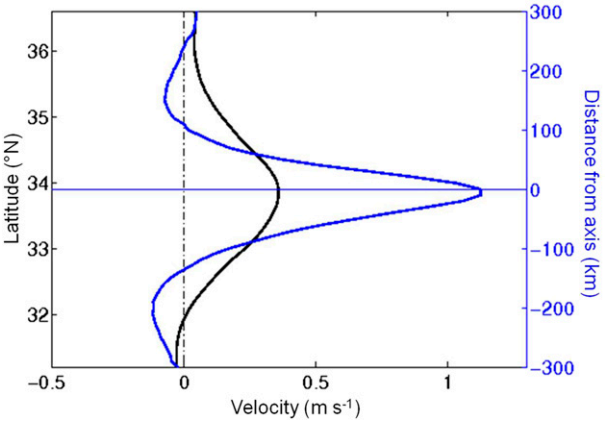

FIG. 4. The 1995–2007 mean cross-jet velocity profile (0–250-m depth average) at 146°E in POP, as computed in the geographic (black) and jet (blue) reference frames. In the geographic reference frame, eastward velocity $\overline{u}$ is plotted; in the jet reference frame, along-jet velocity $\overline{\langle u_j \rangle}^j$ is plotted.

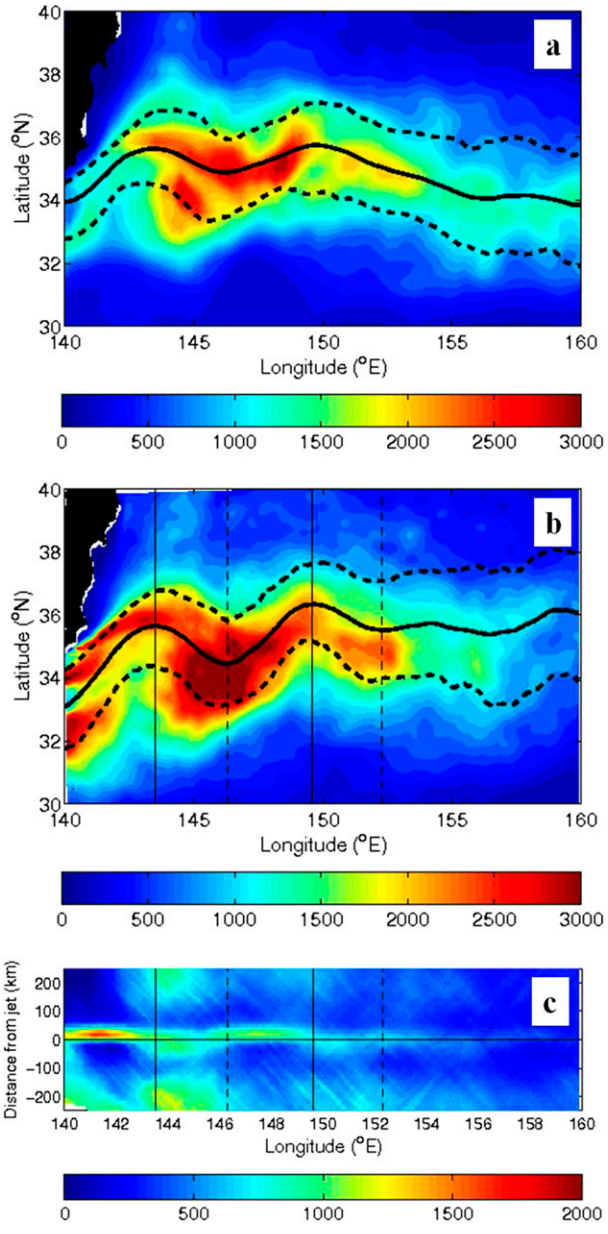

FIG. 5. (a) 1995–2007 geographic mean geostrophic EKE $\overline{|\mathbf{u}|^2}$ from altimetry-derived AVISO-gridded ($\sim 1/3°$) weekly maps of mean sea level anomaly. (b) 1995–2007 geographic mean surface EKE in POP, computed from SSH anomalies, as in (a). The thick black lines indicate the mean (solid) and 10th/90th percentile (dashed) jet axis positions computed from the altimeter, in (a), and POP, in (b), SSH gradients. (c) 1995–2007 jet frame, mean, 0–250-m, depth-averaged EKE $\overline{\langle |\mathbf{u}_j|^2 \rangle^j}$ in POP. The color scales are indicated below each figure. The color scale for (c) is different from (a) and (b).

The forms of the primitive u- and v-momentum equations under hydrostatic and Boussinesq approximations that conserve kinetic energy when discretized in the POP model grid (Smith and Gent 2002; Smith et al. 2010) are

$$\frac{\partial u}{\partial t} + (uu)_x + (vu)_y + (wu)_z - fv = -\frac{1}{\rho_0} p_x + F^x, \quad \text{and} \tag{1}$$

$$\frac{\partial v}{\partial t} + (uv)_x + (vv)_y + (wv)_z + fu = -\frac{1}{\rho_0} p_y + F^y, \tag{2}$$

respectively. The terms F^x and F^y represent all of the effects of external body forcing (such as wind stress) and frictional dissipation. The main distinction between (1) and (2) and the continuous momentum equations is that in the model's discretized grid, momentum is fluxed from one grid cell to the next rather than advected along a fluid parcel trajectory. For example, in the case of u momentum with the three-dimensional del operator ∇_3 and velocity vector $\mathbf{u}_3$, momentum advection is accomplished by $\nabla_3 \cdot (\mathbf{u}_3 u)$ rather than $\mathbf{u}_3 \cdot \nabla_3 u$. The terms in the momentum equations due to the curvature of the model grid (Smith and Gent 2002; Smith et al. 2010) can be neglected, as the study region neither encompasses a large subset of the global grid nor approaches one of its poles.

The curl of (1) and (2) is the vorticity equation

$$\frac{\partial \zeta}{\partial t} + \nabla \cdot \mathbf{\Phi} + (wv)_{xz} - (wu)_{yz} + \beta v + f(u_x + v_y) = F, \tag{3}$$

with the two-dimensional del operator $\nabla = (\partial/\partial x, \partial/\partial y)$, the horizontal flux vector of relative vorticity $\mathbf{\Phi} = \langle (uv)_x - (uu)_y, (vv)_x - (vu)_y \rangle$, and $F = \mathbf{k} \cdot \nabla \times (F^x, F^y)$, the external vorticity forcing and internal dissipation; F is not computed explicitly in our budget but rather is considered a residual. By adding and subtracting $(vw_z)_x - (uw_z)_y$ from the $\nabla \cdot \mathbf{\Phi}$ and $(wv)_{xz} - (wu)_{yz}$ terms, respectively, in (3) and invoking continuity, we obtain a form that more closely resembles a vorticity conservation equation:

$$\frac{\partial \zeta}{\partial t} + \mathbf{u} \cdot \nabla \zeta - \zeta w_z + W + \beta v - f w_z = F, \tag{4}$$

with the horizontal velocity vector $\mathbf{u} = (u, v)$, and $W = w\zeta_z + w_x v_z - w_y u_z$. The W term represents the sum of the vertical vorticity advection and twisting terms that result from taking the curl of vertical momentum advection. Correspondingly, the horizontal advection of relative vorticity $\mathbf{u} \cdot \nabla \zeta$ and stretching of relative vorticity $-\zeta w_z$ both result from taking the curl of horizontal momentum advection.

Equation (4) is then depth averaged from $z = -h$ to $z = 0$, with $h = 250$ m in the open ocean to be consistent with the analysis of jet velocity profiles and EKE (section 3b). In a grid cell that has (or is

adjacent to) bathymetry less than 250 m deep, h is instead the depth of the shallowest bathymetry in that cell or any adjacent cell. By not including depths that are laterally adjacent to land, the vorticity equation excludes areas where the curl of the pressure gradient in the discrete model grid is nonzero (appendix C.2 in Yeager 2013) and retains stretching terms near sloping bathymetry that would otherwise be effectively negated by the boundary condition $w = 0$. Hence, the vorticity equation [(4)] takes the same form over shallower bathymetry, as it does in areas with bathymetry deeper than 250 m [see Bell (1999) for further discussion of this method and how it relates to other forms of the vorticity balance].

a. Geographic vorticity budget and eddy forcing

To provide a context for eddy forcing in the jet reference frame, we first consider the vorticity budget in the more commonly used geographic reference frame. This budget is just the geographic time average of (4), that is, the time mean of each of the vorticity equation terms at a fixed longitude and latitude. The geographic time average is denoted with an overbar (e.g., the time average of a term A is denoted as $\overline{A}$):

$$\overline{\frac{\partial \zeta}{\partial t} + \mathbf{u}\cdot\nabla\zeta - \zeta w_z + W + \beta v - f w_z} = \overline{F}. \tag{5}$$

Figure 6 shows the geographic 1995–2007 time mean of the terms in (5) from POP. The tendency term $\overline{\partial\zeta/\partial t}$ (Fig. 6a) is negligible, as expected for a long-term (in this case, multiyear) time average. Away from the near-coastal shallow bathymetry, the dominant balance in the upper 250 m is $\overline{\mathbf{u}\cdot\nabla\zeta} \sim -\overline{\beta v} + \overline{f w_z}$, with relative vorticity advection compensated for by vertical stretching of planetary vorticity and (to a lesser extent) planetary vorticity advection. The three-way balance is indicative of standing baroclinic lee waves generated by the underlying bathymetry (Mizuno and White 1983), particularly the ridge at ~140°E. Near where the jet crosses 140°E, the vertical stretching term $\overline{f w_z}$ actually has a slightly larger magnitude than the relative vorticity advection term $\overline{\mathbf{u}\cdot\nabla\zeta}$, further implicating a localized bathymetric forcing. Moreover, the sign changes in all three terms along the jet correspond to the locations of quasi-permanent crests and troughs in the KE jet (Figs. 6b,e,f).

The remaining terms appear to be negligible away from the coast, including the relative vorticity stretching $-\overline{\zeta w_z}$ (Fig. 6c), vertical vorticity advection and twisting $\overline{W}$ (Fig. 6d), and even the residual $\overline{F}$ (Fig. 6g). The fact that the residual $\overline{F}$, which encompasses wind stress and internal frictional forcing, is not of leading-order importance suggests that the Kuroshio Extension is largely an inertial jet, even as the gyre that drives it is ultimately wind forced.

To quantify the effect of eddy vorticity forcing on the mean flow in the geographic reference frame, the standard (Reynolds) decomposition of velocity into a time mean and time variable or eddy component is applied:

$$\mathbf{u} = \overline{\mathbf{u}} + \mathbf{u}'. \tag{6}$$

The eddy terms that arise from (5) can then be expressed on the right-hand side of the vorticity equation as a forcing on the mean flow terms. We neglect the eddy terms arising from W, since the total W (Fig. 6d) is negligible:

$$\overline{\mathbf{u}}\cdot\nabla\overline{\zeta} - \overline{\zeta}\,\overline{w_z} + \beta\overline{v} - f\,\overline{w_z} = -\overline{\mathbf{u}'\cdot\nabla\zeta'} + \overline{\zeta' w_z'} + \overline{F}. \tag{7}$$

The sum of the two eddy forcing terms on the right-hand side of (7) is the eddy relative vorticity flux convergence, that is, $-\overline{\mathbf{u}'\cdot\nabla\zeta'} + \overline{\zeta' w_z'} = -\overline{\nabla\cdot(\mathbf{u}'\zeta')}$. The eddy vorticity forcing in the geographic reference frame (Fig. 7) appears to be noisy, dominated by maxima/minima at scales of 1°–2°. Note that the eddy forcing from the $\overline{\zeta' w_z'}$ term is essentially nonexistent away from the coast in the geographic frame (Fig. 7b). However, as we will show below, the corresponding eddy forcing term in the jet reference frame is nonnegligible.

b. Vorticity budget in the jet reference frame

Now, we again consider the terms of the vorticity budget, but averaged in the jet reference frame. Performing this calculation within a curved, moving coordinate system would require numerous additional (error prone) terms to close the budget; we sidestep this issue by computing each individual term in the budget in the native model grid (geographic frame) and then binning and averaging in the jet frame only at the end. Hence, the form of the jet frame vorticity budget that we consider first is simply the jet frame time average applied to the vorticity equation [(4)]:

$$\overline{\left\langle \frac{\partial\zeta}{\partial t}\right\rangle + \langle \mathbf{u}\cdot\nabla\zeta\rangle - \langle\zeta w_z\rangle + \langle W\rangle + \langle\beta v\rangle - \langle f w_z\rangle}^{\,j} = \overline{\langle F\rangle}^{\,j}. \tag{8}$$

Figure 8 illustrates the terms in the 1995–2007 jet frame mean of the vorticity equation [(8)] for all bins within the ranges 140°E $\le \phi \le$ 160°E and $-250 \le d \le$ 250 km. In the jet frame, $\overline{\langle\partial\zeta/\partial t\rangle}^{\,j}$ may be nonnegligible if

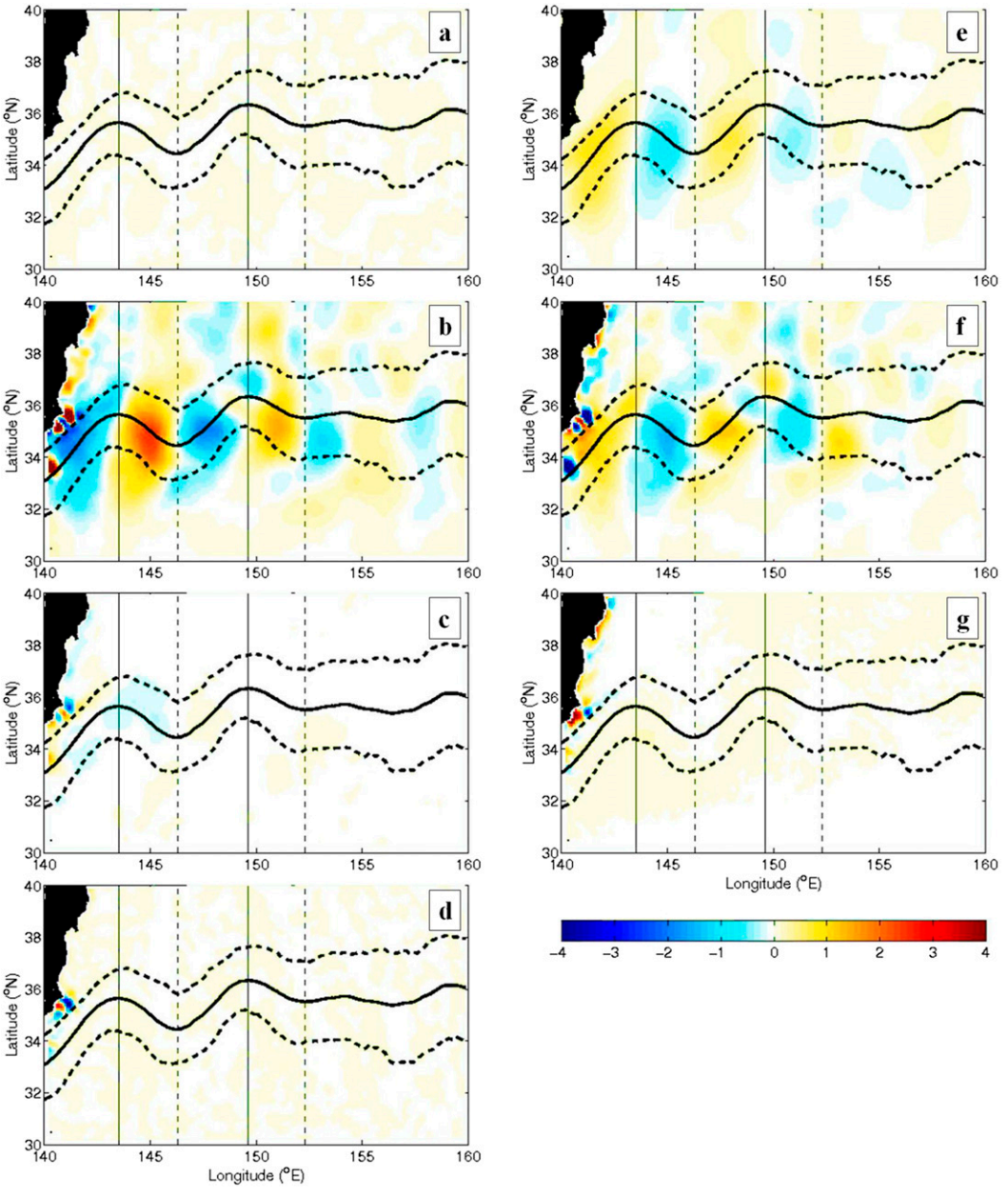

FIG. 6. 1995–2007 geographic time mean of the terms in the full vorticity budget in (5), vertically averaged, 0–250 m, from POP. The terms are the depth- and time-averaged (a) $\overline{\partial\zeta/\partial t}$, (b) $\overline{\mathbf{u}\cdot\nabla\zeta}$, (c) $\overline{-\zeta w_z}$, (d) $\overline{W}$, (e) $\overline{\beta v}$, (f) $\overline{-f w_z}$, and (g) $\overline{F}$, the residual. Each term has been smoothed postaveraging with a Gaussian filter (0.2° e-folding scale, 1° cutoff radius). The e-folding scale and cutoff radius were chosen to remove noise at the highest wavenumbers, while preserving forcing patterns that are evident in the jet at the spatial scales of eddies (1°–2°). Thick black lines indicate the mean (solid) and 10th/90th percentile (dashed) jet axis positions. The thin vertical lines denote the longitudes of crests (solid) and troughs (dashed) in the mean jet path. The color scale is indicated in the lower-right corner and is the same for (a)–(g), with units of $10^{-11}\,\mathrm{s}^{-2}$.

the local ζ tendency is correlated with shifts in the jet position. However, this is not the case in the KE jet, where the jet frame time-mean $\overline{\langle\partial\zeta/\partial t\rangle^j}$ (Fig. 8a) is still negligible.

As in the geographic frame, the jet frame time-mean vorticity budget indicates a three-way dominant balance in which $\overline{\langle\mathbf{u}\cdot\nabla\zeta\rangle^j}$ is compensated by $\overline{\langle\beta v\rangle^j}$ and $-\overline{\langle f w_z\rangle^j}$, representative of standing lee waves. Hence,

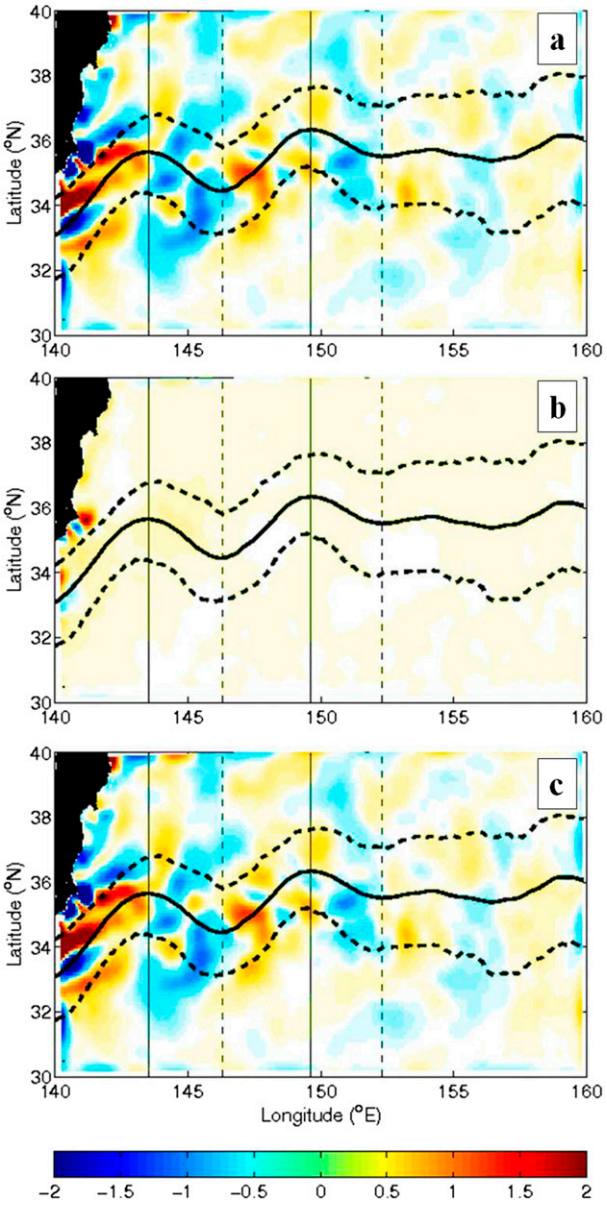

FIG. 7. (a)–(c) 1995–2007 geographic mean eddy forcing terms in (7), vertically averaged 0–250 m from POP. The terms are the depth- and time-averaged (a) $-\overline{\mathbf{u}'\cdot\nabla\zeta'}$, (b) $\overline{\zeta' w_z'}$, and (c) the total eddy forcing $-\overline{\nabla\cdot(\mathbf{u}'\zeta')}$. Each term has been smoothed post-averaging with a Gaussian filter (0.2° e-folding scale, 1° cutoff radius). Thick black lines indicate the mean (solid) and 10th/90th percentile (dashed) jet axis positions. The thin vertical lines denote the longitudes of crests (solid) and troughs (dashed) in the mean jet path. The color scale is indicated at the bottom and is the same for (a)–(c) but different from Fig. 6, with units of $10^{-11}\,\mathrm{s}^{-2}$.

both geographic and jet frame vorticity budgets demonstrate that the bathymetry-induced lee waves are associated with substantial vertical displacements related to the baroclinic structure of these waves. However, the maxima and minima of these terms are of higher magnitude and are spatially more constrained in the jet frame budget than in the geographic budget.

Outside the jet core (approximately 100–200 km from the jet axis) there is a cross-jet asymmetry in the relative vorticity advection (Fig. 8b) and vertical stretching (Fig. 8f) terms that is not readily apparent in the geographic budget (Figs. 6b,f). In these areas on either side of the jet core, the vertical stretching term suggests downwelling south of the jet and upwelling north of the jet. We also note that in the jet frame budget, the $-\overline{\langle\zeta w_z\rangle}^j$ and $\overline{\langle F\rangle}^j$ terms are no longer negligible near the jet axis (Figs. 8c,g), albeit still smaller in magnitude than the three dominant terms. The jet frame residual $\overline{\langle F\rangle}^j$ (Fig. 8g), which encompasses wind stress and frictional forcing and was negligible in the geographic reference frame, has a spatial distribution largely consistent with a biharmonic dissipation of ζ maxima and minima on the flanks of the high velocity jet core.

c. *Eddy forcing in the jet reference frame*

We now expand the jet frame vorticity budget discussed in section 4b to isolate the contribution from transient eddies. Neglecting $\partial\zeta/\partial t$ and W, which were shown to be negligible in the jet frame time-mean vorticity budget (Figs. 8a,d), we apply a jet frame mean-eddy decomposition. When using the jet frame decomposition, computations in the jet frame can no longer be limited to binning and averaging at the end, as was the case with (8). Rather, it is necessary to compute a jet frame mean velocity and project the mean velocity field back onto the model grid at each time. The jet frame eddy velocity at each model grid point and time can then be defined as the difference between the total velocity and the jet frame mean velocity for the (ϕ, d) bin associated with that grid point and time:

$$\mathbf{u}'|_{(\phi,\Theta,t)} \equiv \mathbf{u}|_{(\phi,\Theta,t)} - \overline{\langle\mathbf{u}\rangle}^j|_{(\phi,d)}\,. \tag{9}$$

The jet frame mean velocity $\overline{\langle\mathbf{u}\rangle}^j$, projected onto the axes of the model grid, is computed using a binning and averaging process analogous to the jet frame time averaging for scalar quantities, but rotations are also necessary to average the along-stream and cross-stream components of the vector (see the appendix, section b, for a more detailed description). Substituting the decomposition into the jet frame–averaged vorticity budget [(8)] yields

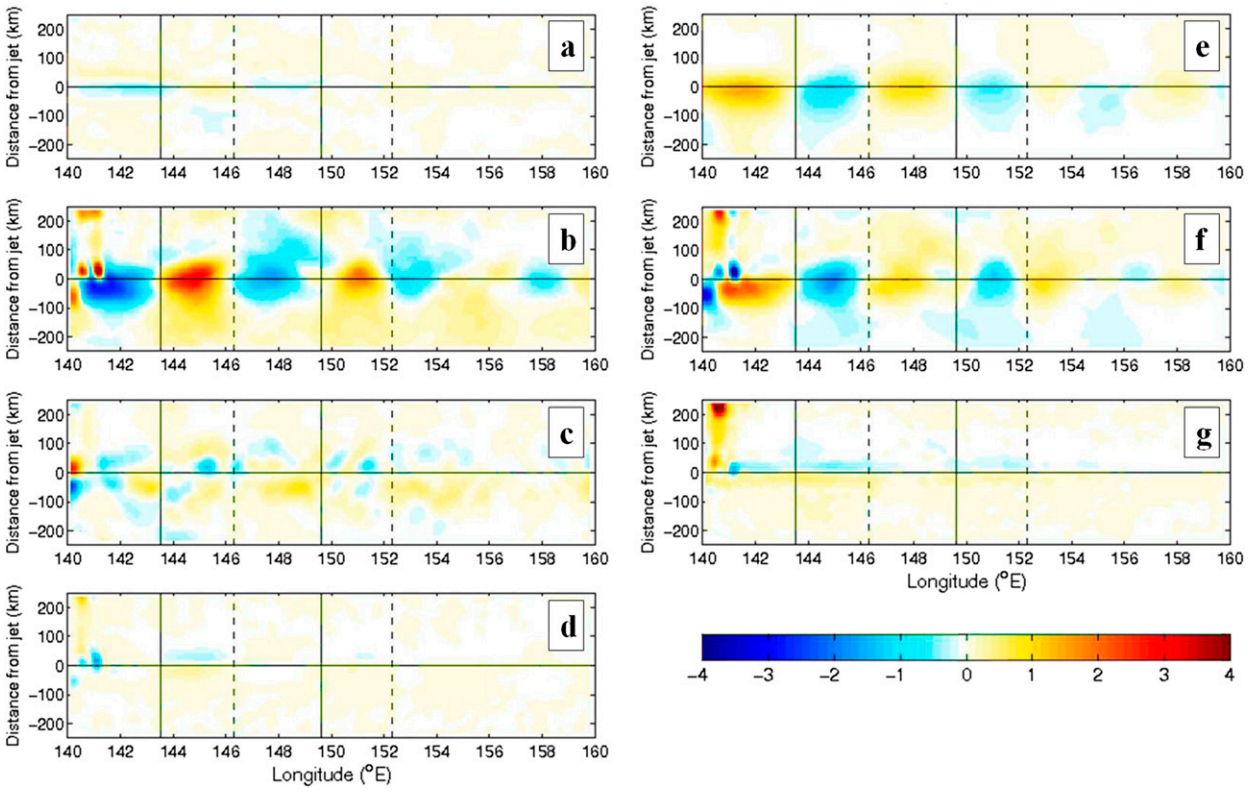

FIG. 8. 1995–2007 jet frame time mean of the terms in the full vorticity budget in (8), vertically averaged 0–250 m from POP. The terms are the depth-averaged and jet frame time-averaged (a) $\overline{\langle \partial\zeta/\partial t\rangle}^{j}$, (b) $\overline{\langle \mathbf{u}\cdot\nabla\zeta\rangle}^{j}$, (c) $\overline{-\langle \zeta w_z\rangle}^{j}$, (d) $\overline{\langle W\rangle}^{j}$, (e) $\overline{\langle \beta v\rangle}^{j}$, (f) $\overline{-\langle fw_z\rangle}^{j}$, and (g) $\overline{\langle F\rangle}^{j}$, the residual. Each term has been smoothed postaveraging with a Gaussian filter (0.2° e-folding scale, 1° cutoff radius). Color scale is indicated in the lower-right corner and is the same for (a)–(g), with units of $10^{-11}\,\mathrm{s}^{-2}$.

$$\overline{\langle\overline{\mathbf{u}}^{j}\cdot\nabla\overline{\zeta}^{j}\rangle-\langle\overline{\zeta}^{j}\overline{w_z}^{j}\rangle+\langle\beta v\rangle-\langle fw_z\rangle+\langle(\mathbf{u}\cdot\nabla\zeta)'\rangle-\langle(\zeta w_z)'\rangle}^{j}=\overline{\langle F\rangle}^{j},\tag{10}$$

with $\overline{\zeta}^{j}\equiv(\overline{\langle v\rangle}^{j})_x-(\overline{\langle u\rangle}^{j})_y$, $\overline{w_z}^{j}\equiv-(\overline{\langle u\rangle}^{j})_x-(\overline{\langle v\rangle}^{j})_y$, and the eddy terms given by

$$(\mathbf{u}\cdot\nabla\zeta)'=\mathbf{u}\cdot\nabla\zeta-\overline{\langle\mathbf{u}\rangle}^{j}\cdot\nabla\overline{\zeta}^{j},\quad\text{and}\tag{11}$$

$$(\zeta w_z)'=\zeta w_z-\overline{\zeta}^{j}\overline{w_z}^{j}.\tag{12}$$

All spatial derivatives, including those contained in the gradient operator ∇, are calculated in the (Eulerian) native model grid; this precludes the need to introduce additional terms into the vorticity budget that are a function of the motion, orientation, or curvature of the reference frame. It is important to note that in the jet frame, spatial derivatives do not commute with the time averages, that is, $(\overline{\langle u\rangle}^{j})_x\neq\overline{\langle u_x\rangle}^{j}$. Thus, $(\mathbf{u}\cdot\nabla\zeta)'\neq\mathbf{u}'\cdot\nabla(\zeta-\overline{\zeta}^{j})$ and $(\zeta w_z)'\neq(\zeta-\overline{\zeta}^{j})\cdot(w_z-\overline{w_z}^{j})$.

As in the geographic case, the eddy terms in (10) can now be expressed as a forcing on the mean flow:

$$\overline{\langle\overline{\mathbf{u}}^{j}\cdot\nabla\overline{\zeta}^{j}\rangle-\langle\overline{\zeta}^{j}\overline{w_z}^{j}\rangle+\langle\beta v\rangle-\langle fw_z\rangle}^{j}=\overline{-\langle(\mathbf{u}\cdot\nabla\zeta)'\rangle+\langle(\zeta w_z)'\rangle+\langle F\rangle}^{j}.\tag{13}$$

The eddy relative vorticity advection $\overline{-\langle(\mathbf{u}\cdot\nabla\zeta)'\rangle}^{j}$ and eddy vertical stretching of relative vorticity $\overline{\langle(\zeta w_z)'\rangle}^{j}$ on the right-hand side of (13) may now be considered forcing terms on the mean flow. The sum of the two eddy forcing terms $\overline{-\langle(\mathbf{u}\cdot\nabla\zeta)'\rangle}^{j}+\overline{\langle(\zeta w_z)'\rangle}^{j}=-\overline{\langle[\nabla\cdot(\mathbf{u}\zeta)]'\rangle}^{j}$ is the horizontal eddy vorticity flux convergence, which composes the total eddy forcing considered in this study. The residual $\overline{\langle F\rangle}^{j}$ in (13) is the same as for the full jet frame vorticity budget in (8), with a forcing that acts to damp strong ζ maxima/minima in the jet (Fig. 8g).

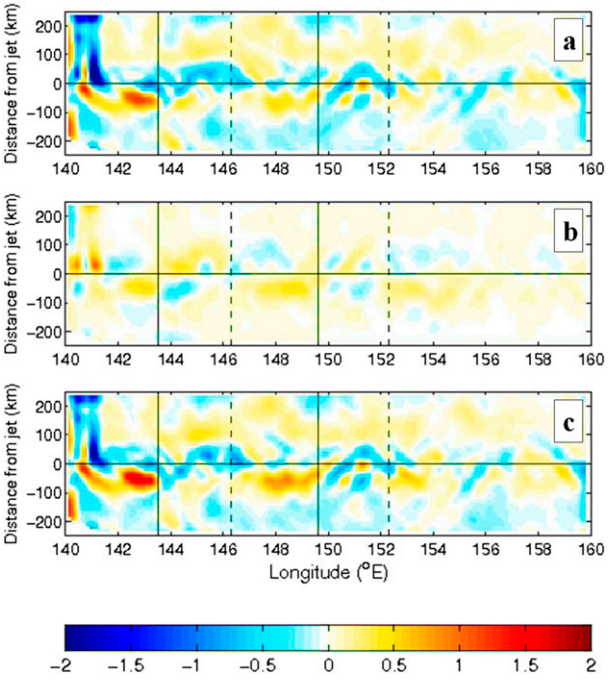

FIG. 9. (a)–(c) 1995–2007 jet frame, mean eddy forcing terms in (13), vertically averaged 0–250 m from POP. The terms are the depth-averaged and jet frame time-averaged (a) $\overline{-\langle(\mathbf{u}\cdot\nabla\zeta)'\rangle^{j}}$, (b) $\overline{\langle(\zeta w_z)'\rangle^{j}}$, and (c) the total eddy forcing $\overline{\langle-[\nabla\cdot(\mathbf{u}\zeta)]'\rangle^{j}}$. Each term has been smoothed postaveraging with a Gaussian filter (0.2° e-folding scale, 1° cutoff radius). Color scale is indicated at the bottom and is the same for (a)–(c) but different from Fig. 8, with units of $10^{-11}\,\mathrm{s}^{-2}$.

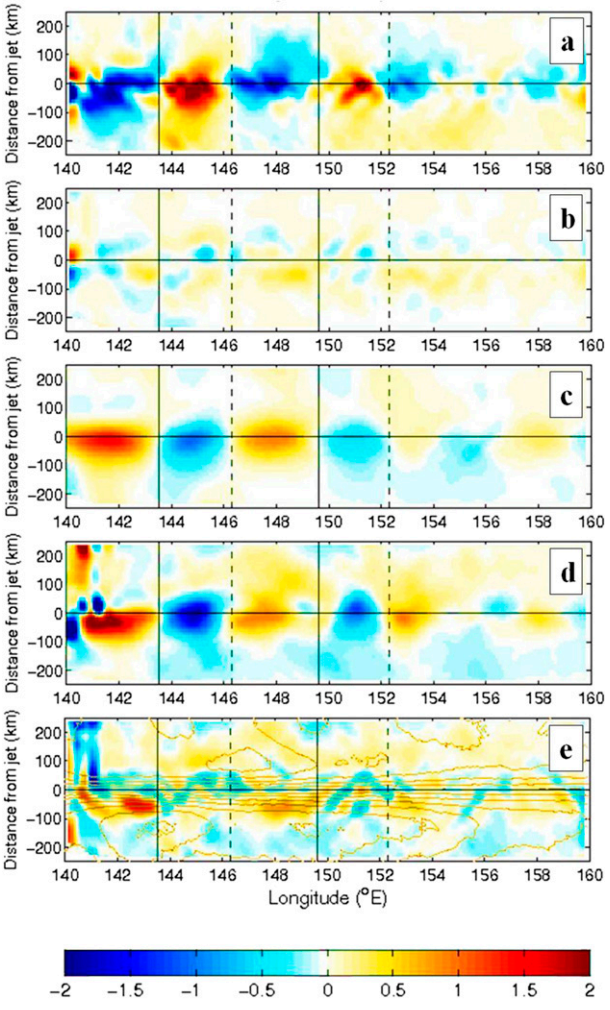

FIG. 10. 1995–2007 jet frame mean circulation terms in the vorticity budget in (13). The mean circulation terms are (a) $\langle\overline{\mathbf{u}}^{j}\cdot\nabla\overline{\zeta}^{j}\rangle$, (b) $\overline{-\langle\overline{\zeta}^{j}\overline{w_z}^{j}\rangle}^{j}$, (c) $\langle\beta v\rangle^{j}$, and (d) $\overline{-\langle fw_z\rangle^{j}}^{j}$. (e) The total eddy forcing $\overline{\langle-[\nabla\cdot(\mathbf{u}\zeta)]'\rangle^{j}}$, with superimposed 1995–2007 jet frame mean SSH (thin brown contours, with a contour interval of 10 cm). Each term has been smoothed postaveraging with a Gaussian filter (0.2° e-folding scale, 1° cutoff radius). Color scale is indicated below (e) and is the same for (a)–(e), with units of $10^{-11}\,\mathrm{s}^{-2}$.

As in the geographic case, the jet frame eddy forcing terms in (13), computed along the KE jet (Fig. 9), exhibit small-scale noise, particularly within 50 km of the jet axis. Nonetheless, the jet frame eddy forcing distribution can be much more readily associated with plausible dynamical mechanisms than the geographic eddy forcing. To aid the interpretation of the eddy forcing, we compare the total eddy forcing with the vorticity budget terms that represent the mean flow (Fig. 10). A qualitative comparison of the patterns in Fig. 10 is supplemented with spatial correlations and projections of the mean terms onto the total eddy forcing (Table 1), as a first-order attempt to quantify how much of the mean circulation (as indicated by vorticity) is eddy driven. The correlations and projections in Table 1 are computed separately for the high velocity jet core and for the regions outside the jet core, as the vorticity balances in these areas are quite different. In the high velocity jet core, the eddy forcing is most highly correlated with the mean relative vorticity advection $\langle\overline{\mathbf{u}}^{j}\cdot\nabla\overline{\zeta}^{j}\rangle$ and mean vertical stretching $-\overline{\langle fw_z\rangle^{j}}^{j}$ terms, while outside the jet core only the mean vertical stretching term $-\overline{\langle fw_z\rangle^{j}}^{j}$ is robustly correlated with the forcing. The projections similarly indicate that these two mean circulation terms account for most of the flow's adjustment to the influence of eddies. The spatial variations in eddy forcing and their implications for the mean circulation of the KE jet and its recirculation gyres are discussed further in section 5.

5. Eddy forcing patterns

The eddy forcing of the mean flow in the jet reference frame (Figs. 9, 10) may be largely explained as the superposition of four patterns, represented schematically in Fig. 11. The first three of these patterns only act within the KE jet itself and are mainly balanced by the mean $\langle\overline{\mathbf{u}}^{j}\cdot\nabla\overline{\zeta}^{j}\rangle$ relative vorticity advection and $-\overline{\langle fw_z\rangle^{j}}^{j}$

TABLE 1. Correlations and projections of mean terms M in the jet frame vorticity budget with the total eddy forcing $E = \overline{\langle -[\nabla \cdot (\mathbf{u}\zeta)]' \rangle}^{j}$. Both M and E first have cross-jet means at each longitude removed to focus on the cross-jet varying part of the vorticity forcing that decelerates/accelerates the jet. The correlation of M with E is then given by $r_{ME} = [1/(\sigma_M \sigma_E)] \sum_i \sum_j M_{ij} E_{ij}$. The indicated p values are for the correlation coefficients r_{ME}, using the one-tailed Student's t test (Emery and Thomson 2001), with effective degrees of freedom determined based on the decorrelation scale of the total eddy forcing in the region indicated. The forcing-normalized projection of M onto E is given by $P_{ME} = (1/\sigma_E^2) \sum_i \sum_j M_{ij} E_{ij} = r_{ME} * (\sigma_M / \sigma_E)$, with σ_X indicating the standard deviation of X. The normalization is such that the sum of the P_{ME} for all M terms is 1, though not all M terms are included below.

	Mean term M	Correlation r_{ME}	One-tailed p value	Forcing-normalized projection P_{ME}
Within jet core	$\overline{\langle \overline{\langle \mathbf{u} \rangle}^{j} \cdot \nabla \overline{\zeta}^{j} \rangle}^{j}$	0.45	2×10^{-9}	0.47
(-100 km $< d <$ 60 km)	$\overline{-\langle \overline{\zeta}^{j} \overline{w_z}^{j} \rangle}^{j}$	0.38	8×10^{-7}	0.10
	$\overline{\langle \beta v \rangle}^{j}$	0.28	3×10^{-4}	0.11
	$\overline{-\langle f w_z \rangle}^{j}$	0.47	2×10^{-10}	0.40
Outside of jet core	$\overline{\langle \overline{\langle \mathbf{u} \rangle}^{j} \cdot \nabla \overline{\zeta}^{j} \rangle}^{j}$	0.10	0.33	0.10
(-240 km $\leq d \leq -100$ km or 60 km $\leq d \leq$ 200 km)	$\overline{-\langle \overline{\zeta}^{j} \overline{w_z}^{j} \rangle}^{j}$	0.34	0.06	0.09
	$\overline{\langle \beta v \rangle}^{j}$	0.21	0.17	0.09
	$\overline{-\langle f w_z \rangle}^{j}$	0.63	5×10^{-4}	0.55

vertical stretching terms (Fig. 10; Table 1). The fourth pattern predominates on either side of the jet where the recirculation gyres are present and is primarily balanced by the $-\overline{\langle f w_z \rangle}^{j}$ vertical stretching term.

Focusing first on the eddy horizontal advection forcing term $-\overline{\langle (\mathbf{u} \cdot \nabla \zeta)' \rangle}^{j}$ (Fig. 9a), a superposition of two patterns is apparent. Pattern 1 (Fig. 11a) is generally positive vorticity forcing to the south and negative vorticity forcing to the north. This corresponds to a downgradient vorticity flux across the jet, such that the eddies are acting to reduce the cross-jet vorticity contrast and decelerate the jet. Such behavior is characteristic of developing instabilities along a barotropic jet (Waterman and Jayne 2011; Waterman and Hoskins 2013). Pattern 2 (Fig. 11b), again originating from the $-\overline{\langle (\mathbf{u} \cdot \nabla \zeta)' \rangle}^{j}$ term, is a tendency of the vorticity forcing to be more positive in northward-flowing parts of the mean jet (e.g., 140°–143°E) and more negative in southward-flowing parts of the mean jet (e.g., 144°–146°E). Pattern 2 is compensated for by both $-\overline{\langle f w_z \rangle}^{j}$ and $\overline{\langle \beta v \rangle}^{j}$ (Figs. 10c,d) in the mean flow, suggesting that eddies play a role in reinforcing the stretching and meridional motions associated with the quasi-permanent meanders in the jet; this result is consistent with estimates of eddy forcing derived from satellite observations (Qiu and Chen 2010).

Pattern 3 (Fig. 11c) originates from the $\overline{\langle (\zeta w_z)' \rangle}^{j}$ term (Fig. 9b) and consists of both cross-jet and along-jet variations in vorticity forcing. Approximately where the mean jet is flowing northward, the vorticity forcing is positive south of and negative north of the jet axis, reinforcing pattern 1 and the associated downgradient fluxes (corresponding to jet deceleration). Where the mean jet is flowing southward, however, the vorticity forcing pattern is the opposite—negative to the south and positive to the north of the jet. This pattern indicates upgradient vorticity fluxes and an acceleration of the jet. Pattern 3's acceleration of the jet is partially canceled out by pattern 1 in the $-\overline{\langle \overline{\langle \mathbf{u} \rangle}^{j} \cdot \nabla \overline{\zeta}^{j} \rangle}^{j}$ term (Fig. 10a), but in some areas its effect persists (e.g., at ~144°E).

The effect of pattern 3 may be further clarified by considering the change in along-jet velocity from west to east (Fig. 12). A general deceleration of the jet occurs east of a maximum at 142°E, which reflects the influence of both eddy forcing patterns 1 and 3 as well as frictional dissipation. However, at 144°–145°E and 150°–151°E, the opposite occurs: a brief acceleration of the jet toward the east. Both of these locations are immediately downstream of crests in the long-term mean jet (Fig. 9d), and both coincide with the eddy acceleration from the $\overline{\langle (\zeta w_z)' \rangle}^{j}$ term (Fig. 9b). The acceleration of the jet at these locations thus appears to be closely related to vertical vortex stretching, likely from some combination of eddy motions and sharp curves (i.e., ζ anomalies) in the jet itself. The locations of these eddy-forced accelerations in the jet are approximately coincident with negative (upgradient), cross-stream eddy diffusivities in the upper ocean, as quantified using the same high-resolution configuration of the POP model (Chen et al. 2014). Moreover, studies in the Gulf Stream have observed near-surface, cross-stream divergences (convergences) that are

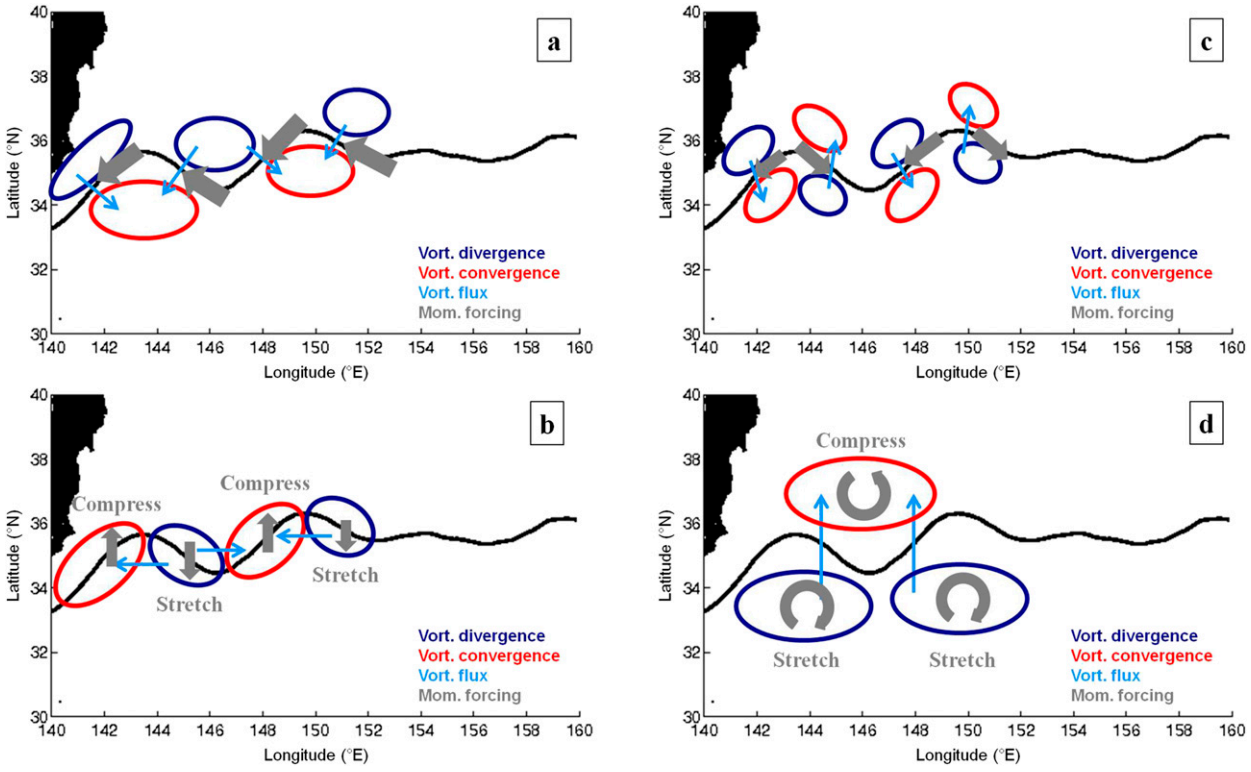

FIG. 11. Schematic of eddy forcing patterns on the mean flow in the KE jet region; subplots show (a) pattern 1 refers to jet core deceleration, (b) pattern 2 refers to meander reinforcement, (c) pattern 3 refers to intermittent jet core acceleration, and (d) pattern 4 refers to forcing of recirculation gyres. The black line indicates the mean path of the KE jet. Ellipses indicate areas of eddy vorticity convergence (red) and divergence (dark blue), with the implied direction of eddy vorticity fluxes given by light blue arrows. The thick gray arrows illustrate the effective directions of the eddy momentum forcing from each pattern. Gray text indicates the vertical deformation of the upper layer because of the influence of the eddy forcing pattern.

situated upstream (downstream) of a meander crest (Bower 1989; Thomas and Joyce 2010), consistent with the alternating deceleration and acceleration of the jet associated with pattern 3. Bower and Rossby (1989) observed entrainment of fluid from outside the jet near crests but not near troughs, likewise suggesting an asymmetry in flow properties relating to the jet's meanders. Thomas and Joyce (2010) noted that the cross-stream convergence downstream of a jet crest is frontogenetic; the eddy forcing described in pattern 3 suggests that mesoscale instabilities help support frontogenesis in these locations.

The along-jet transitions in eddy forcing represented in pattern 3 also resemble in some aspects the downstream changes identified in idealized quasigeostrophic (QG) studies of barotropic (e.g., Jayne et al. 1996; Waterman and Hoskins 2013) and baroclinic (e.g., Holland and Rhines 1980; Mizuta 2009; Waterman and Jayne 2011) zonal jets. In the idealized studies, eddies develop from unstable regions in the mean flow, with downgradient eddy vorticity fluxes acting to decelerate the mean eastward jet. However, downstream of the unstable regions, the QG jet stabilizes and resembles a wave radiator, with advected and radiating instabilities inducing net upgradient eddy vorticity fluxes (e.g., Holland and Rhines 1980; Waterman and Jayne 2011) that help to drive the mean eastward jet and its recirculation gyres. This would appear to offer an explanation for the along-jet variations in eddy acceleration of the jet but does not explain why the eddy-induced eastward accelerations only appear in the $\overline{\langle(\zeta w_z)'\rangle}^{j}$ term. In the case of the barotropic jet, the only nonnegligible eddy forcing term to decelerate/accelerate the mean jet is $-\overline{\langle\overline{\mathbf{u}}\rangle^{j}\cdot\nabla\overline{\zeta}^{j}}^{j}$, but in this case it is the $\overline{\langle(\zeta w_z)'\rangle}^{j}$ stretching term that supplies the alternating deceleration and acceleration. Aside from this difference, our results show eddy–mean flow interactions similar to those in idealized QG zonal jets, with some additional complexity associated with the quasi-permanent meanders of the KE.

Pattern 4 (Fig. 11d) is the dominant eddy forcing more than 80 km from the jet axis, originating from the $-\overline{\langle\overline{\mathbf{u}}\rangle^{j}\cdot\nabla\overline{\zeta}^{j}}^{j}$ term; it consists of negative forcing south of the jet and positive forcing north of the jet. As this forcing is balanced mostly by $-\overline{\langle fw_z\rangle}^{j}$ (Fig. 10; Table 1), the

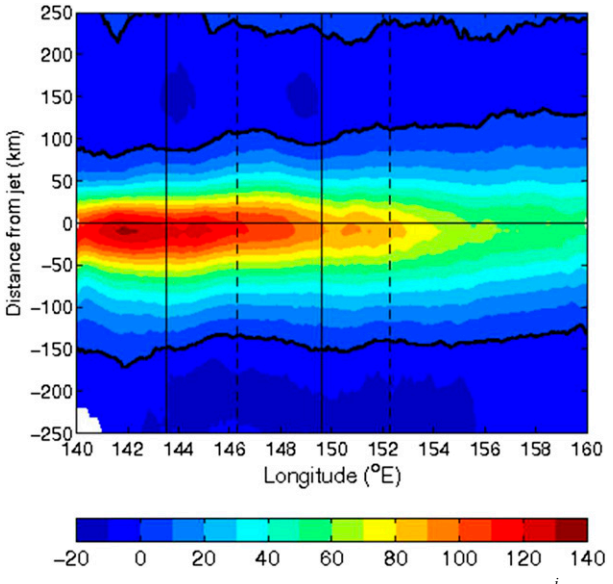

FIG. 12. 1995–2007 jet frame mean along-jet velocity $\overline{\langle u_j \rangle}^j$, vertically averaged 0–250 m from POP. The aspect ratio is distorted to highlight the along-jet changes in $\overline{\langle u_j \rangle}^j$. The color scale is indicated at the bottom, with units of cm s^{-1}.

primary consequence of eddy vorticity forcing outside of the KE jet core is mean vertical stretching of the surface layer to the south of the jet and mean vertical compression to the north of the jet. The baroclinic adjustment to these changes could help maintain the pressure anomalies that drive the recirculation gyres—implying that eddies do indeed help drive the broader mean recirculations, even as the eddy forcing is mostly against the mean flow at the jet axis. The mean and eddy forcing terms also may be used to consider whether recirculation gyres are driven by the mean advection of PV anomalies from other latitudes or by eddy motions [for a more detailed discussion see Waterman and Jayne (2011)]. If mean PV advection is the dominant mechanism, then the vertical stretching $-\overline{\langle f w_z \rangle}^j$ (Fig. 10d) north and south of the jet should be compensated by the mean relative vorticity advection $\overline{\langle \overline{\mathbf{u}}^j \cdot \nabla \bar{\zeta}^j \rangle}^j$ (Fig. 10a). Partial compensation between these mean terms is shown in some areas south of the jet, particularly east of 150°E and between 144° and 146°E (Figs. 10a,d). However, in other regions outside the jet core, mean vorticity advection does not seem capable of inducing vertical stretching of the correct sign; only the eddy forcing (Fig. 10e) acts consistently to stretch (compress) the upper-layer south (north) of the jet core, supporting the hypothesis that the recirculations are largely eddy driven (e.g., Jayne et al. 1996; Waterman and Jayne 2011).

6. Jet instability characteristics

One possible mechanism for generating eddy activity and eddy forcing is a background state of the jet that is unstable to small perturbations. An extensive literature considers the growing and radiating modes of instability for barotropic (e.g., Kuo 1949; Howard and Drazin 1964; Talley 1983a) and baroclinic (e.g., Talley 1983b; Samelson and Pedlosky 1990) instabilities. Here, we note locations where the mean state of the jet allows for, but does not necessarily support, unstable modes. A necessary condition for baroclinic instability (Charney and Stern 1962) is a change in sign of the Ertel PV gradient along isopycnal Q_y, in the cross-jet direction. For a zonal jet, Q_y is given by

$$Q_y \equiv -\frac{\rho}{(\rho_\theta)_z}\left\{\frac{\partial Q_E}{\partial y} - \frac{\partial Q_E}{\partial z}\left[\frac{(\rho_\theta)_y}{(\rho_\theta)_z}\right]\right\}, \tag{14}$$

where $Q_E \equiv -[(f+\zeta)/\rho](\rho_\theta)_z$ is Ertel PV, ρ_θ is potential density, with the Coriolis parameter f and relative vorticity $\zeta = v_x - u_y$. The expanded form of Q_y is

$$Q_y = (\beta + \zeta_y) + (f+\zeta)\frac{(\rho_\theta)_{zy}}{(\rho_\theta)_z} + f\frac{(\rho_\theta)_{zz}(\rho_\theta)_y}{[(\rho_\theta)_z]^2} + \zeta_z\left[\frac{(\rho_\theta)_y}{(\rho_\theta)_z}\right], \tag{15}$$

with $\beta = \partial f/\partial y$ as the planetary vorticity gradient. For a jet such as the KE that is generally nonzonal at a given location, the meridional y derivatives in (14) and (15) are instead computed in the cross-jet direction. If ζ and its gradients are negligible, then this condition is equivalent to the baroclinic instability condition in Gill et al. (1974). If isopycnals are flat (i.e., $(\rho_\theta)_y = 0$), then (15) reduces to the barotropic instability condition that $\partial/\partial y(f+\zeta)$ must change sign in the cross-jet direction.

Transects (Figs. 13a–c) of the jet at 142°E (northward mean jet and longitude of regional jet frame EKE maximum in Fig. 5c), 145°E (southward mean jet), and 148°E (northward mean jet) illustrate a notable asymmetry of the KE jet's mean background state. While the PV gradient Q_y (Figs. 13d–f) in the upper 100 m reverses on both flanks of the jet, only the gradient reversal on the north flank extends down to the thermocline and beyond. On the south flank of the jet, a strong positive gradient in Ertel PV at 100–500 m exists between the low PV subtropical mode water south of the jet and the jet axis, consistent with observations of PV structure across the KE jet (Howe et al. 2009). The strong positive PV gradient stabilizes the southern flank of the jet—likely explaining the minima in jet frame EKE immediately south of the jet axis (Fig. 5c). Because of the stabilizing PV gradient in the isopycnal range ρ_θ = 1024.5–1026.0 kg m^{-3} (Figs. 13d–f), the reversals in Q_y on the south flank of the jet are displaced further from the jet axis than on the north flank, well outside the region of

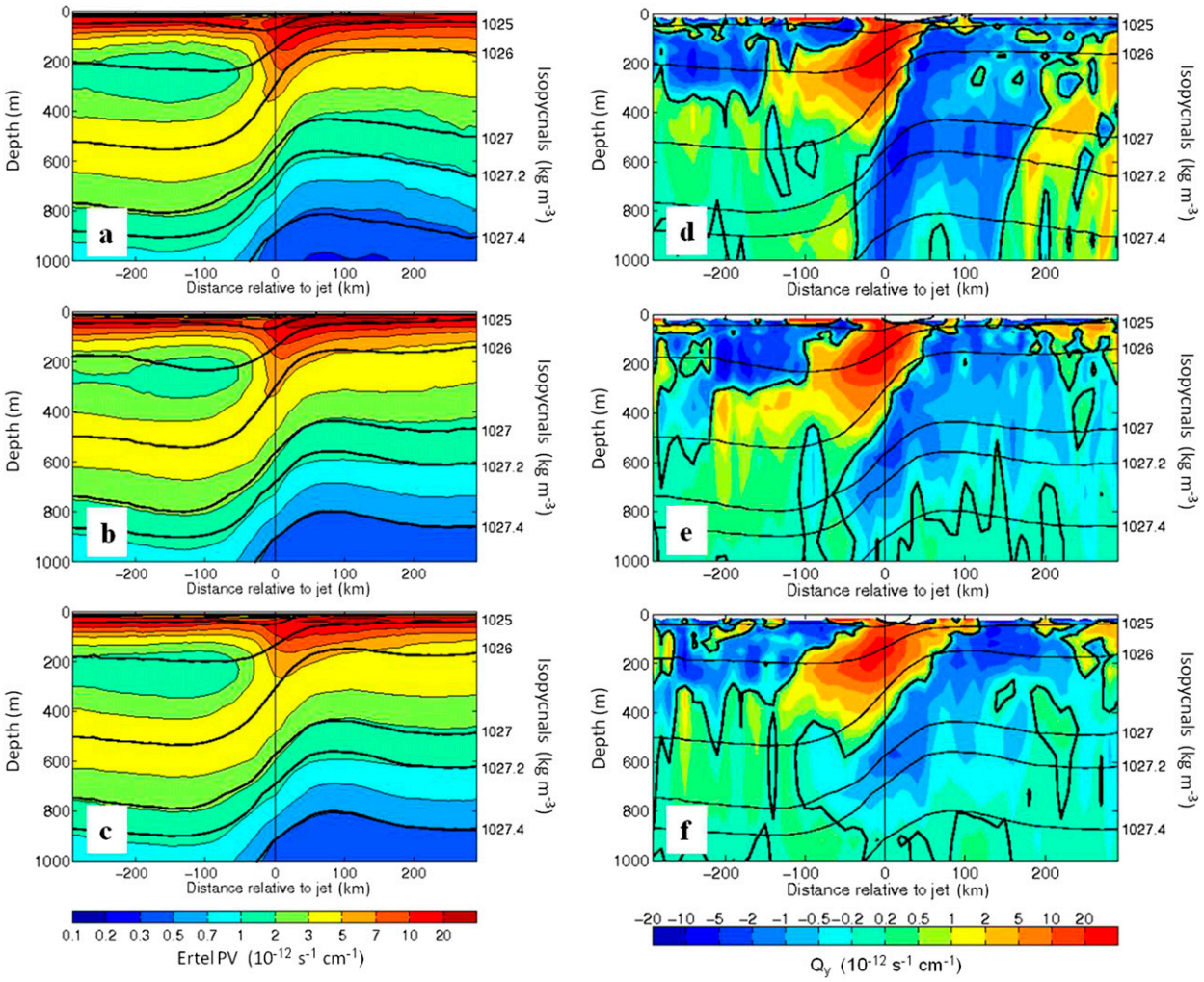

FIG. 13. Transects of Ertel potential vorticity from POP, 1995–2007 mean, with isopycnals (black contours) of potential densities relative to the surface (labeled on right axis) at (a) 142°E, (b) 145°E, and (c) 148°E. The color scale is indicated below (c) and is approximately logarithmic. (d)–(f) As in (a)–(c), but colors indicate cross-jet gradient of Ertel potential vorticity Q_y along isopycnals. Thick black contours indicate zero crossings of Q_y, corresponding to reversals in the along-isopycnal Ertel PV gradient. The color scale is indicated below (f) and is approximately logarithmic for both negative and positive values of Q_y.

high velocity and high shear. This may be related to the jet frame EKE asymmetry (Fig. 5c), as much of the jet frame EKE is confined to the north flank of the jet.

As the jet flows eastward from 142° (Fig. 13d) to 148°E (Fig. 13f), the zero crossing of Q_y on the north flank moves further from the high velocity jet core and its associated shear. Thus, a gradual lessening of the positive and negative Q_y gradients occurs north of the jet axis, consistent with the dampening magnitude of jet frame EKE maxima as the jet moves eastward. However, the most favorable conditions for baroclinic instability remain to the north of the jet in all transects, where the PV gradient reversal is still closer to the jet in the 100–500-m depth range. This does not explain why EKE is higher south of the jet at 145°E (Fig. 5c), though it must be noted that the synoptic stability characteristics of the jet vary with time, and episodic shifts in the jet's asymmetric structure might explain a shift in EKE structure. Yet, the along-jet variation in jet frame EKE (and eddy forcing; i.e., patterns 2 and 3 discussed in section 5) does not appear to result from along-jet changes in the baroclinic instability criterion, suggesting that the jet frame EKE at 144°–145°E may not be generated by the mean background state of the jet.

While the PV gradient is inconclusive regarding the along-jet variations in jet frame EKE, a comparison of the geographic versus jet frame EKE provides more insight. The EKE maximum just south of the mean jet at 144°–145°E is particularly large in the geographic frame (Fig. 5b) compared to the jet frame (Fig. 5c), while the

jet frame does not remove as much eddy variability from the EKE maximum at 142°–143°E. This suggests that the jet position has a more variable distribution at 144°–145°E. The jet frame EKE also has large, well-defined maxima approximately 200 km away from the jet in either direction, which suggests that 144°–146°E is a favored area for ring separation from the jet. Hence, the displacement of the near-jet EKE maximum south of the jet at 144°–146°E (Fig. 5c) may be related to the complicated dynamics of the jet as rings separate from it.

7. Conclusions

In this study, we computed a vorticity budget from the archived output of an ocean GCM using a jet-following reference frame to elucidate eddy–mean interactions that might be partially or even fully obscured in geographic time averages. With this high-resolution model simulation, we show vorticity signatures consistent with some previously observed and explained phenomena in the KE jet: the quasi-permanent meanders that are essentially standing lee waves forced by bathymetry (White and McCreary 1976; Mizuno and White 1983) and the eddies playing a role in driving the time-mean recirculations (e.g., Jayne et al. 1996; Waterman and Jayne 2011). In addition, the jet frame time mean illustrates a fundamental asymmetry of instability development in the KE. The EKE maxima in the jet frame (Fig. 5c) occur on the north side of the jet, opposite regions of nearly zero EKE on the south side. The asymmetry can be readily explained by baroclinic instability criteria in the jet derived from observations (Howe et al. 2009) as well as in our model (Fig. 13), yet this asymmetry is not at all obvious from long-term means of geographic EKE (Figs. 5a,b). The jet frame EKE asymmetry is also consistent with other GCM studies (Qiu et al. 2008; Taguchi et al. 2010) that indicate eddy dissipation processes are necessary to simulate a realistically weak northern recirculation gyre. Our budget also demonstrates eddy forcing behaviors near the KE jet axis that have previously been suggested by idealized models of zonal jets or by observations but have not been explicitly identified in GCMs. In particular, eddies were found to play a role in the acceleration of the high velocity jet core just downstream of quasi-permanent crests in the jet, in contrast to the general decelerating trend of the jet toward the east (Figs. 11c, 12).

It is important to note that the patterns of eddy vorticity forcing identified in this study may not include all of the effects of mesoscale eddies on the vorticity structure of the jet. Rather, the primary focus of this study is on the role of eddies in the forward acceleration/deceleration of the jet and the changes in the cross-jet gradient associated with these velocity changes. In the high velocity jet core surrounding the jet axis, these effects can largely be described in terms of varicose modes of variability, which affect the jet's width and cross-jet structure. Fluctuations in the jet path, which correspond closely if not exactly to sinuous modes of variability, are regarded in the jet frame as part of the mean flow at weekly or longer time scales. (For more background on sinuous and varicose modes, a number of previous studies have considered their stability characteristics using analytical methods; e.g., Talley 1983a,b; Pratt et al. 1991; Hogg 1994). Thus, the jet frame EKE and eddy forcing can be attributed mostly to varicose modes; the effects of sinuous modes are manifested in the mean circulation terms. Both sinuous and varicose modes may radiate instabilities away from the jet (Talley 1983a,b), and the effects of sinuous modes may be quantified as eddy forcing outside the high velocity jet core. Therefore, the jet frame mean-eddy decomposition implemented in this study is most useful for considering the effects of time-variable motions associated with 1) locally growing barotropic and baroclinic instabilities that excite varicose modes of variability as well as sinuous modes that may radiate away from the jet; 2) frontal waves that propagate in the along-jet direction, which may involve varicose modes; and 3) entrant eddies that originate outside of the jet or leave the jet and then impinge on the jet again, such as deep topographically controlled eddies (Tracey et al. 2012; Greene et al. 2012) whose structure is largely independent of the surface jet. Synoptic snapshots suggest that all three types of variability may contribute to the eddy forcing patterns we have identified in the Kuroshio Extension, though substantially more analysis would be needed to quantify the relative impact of each phenomenon on the 13-yr averages of eddy forcing.

One limitation of using eddy vorticity forcing to understand eddy–mean flow interactions is that it is not always a straightforward task to infer the horizontal momentum forcing on the jet. For example, a gyre in near-solid body rotation has negligible relative vorticity gradients $\nabla\zeta \sim 0$ but can still experience nonlinear momentum advection from the wind or eddies spinning up the gyre. The effect of this forcing on the mean flow will appear in the vorticity budget [(7)] or in (13) in the mean stretching terms $-fw_z$ and $-\zeta w_z$; baroclinic adjustment must then be assumed before this forcing has an effect on the horizontal velocity. This issue is of little consequence near the jet where relative vorticity is effectively the cross-jet gradient of along-jet velocity $\overline{\langle u \rangle}^j$, and momentum forcing can be directly inferred from vorticity forcing. Further away from the jet axis, however, the influence of the eddies on the recirculation gyres is only identified indirectly through the response of the $-\overline{\langle fw_z \rangle}^j$ term to eddy forcing. The residual-mean

momentum equations (e.g., Andrews and McIntyre 1976; Young 2012) may be one solution to this problem, in which the eddy forcing is expressed directly in terms of Eliassen–Palm fluxes and is balanced by the acceleration of the mean velocity and a ''residual'' circulation. Applying this framework to a curved, time-variable jet reference frame also presents some challenges, but the ability to compare the acceleration of the mean jet to the eddy momentum forcing makes this an ideal subject for future work.

Acknowledgments. A. S. Delman (ASD) and J. L. McClean (JLM) were supported by NSF Grant OCE-0850463 and Office of Science (BER), U.S. Department of Energy, Grant DE-FG02-05ER64119. ASD and J. Sprintall were also supported by a NASA Earth and Space Science Fellowship (NESSF), Grant NNX13AM93H. JLM was also supported by U.S. DOE Office of Science grant entitled ''Ultra-High Resolution Global Climate Simulation'' via a Los Alamos National Laboratory subcontract. S. R. Jayne was supported by NSF Grant OCE-0849808. Computational resources for the model run were provided by NSF Resource Grants TG-OCE110013 and TG-OCE130010. Output from this simulation is available through the Extreme Science and Engineering Discovery Environment (XSEDE). The authors also acknowledge useful discussions with Larry Pratt and Paola Cessi during the course of this work and the editor, two anonymous reviewers, and an associate editor whose suggestions greatly improved this manuscript.

APPENDIX

A Longitude-Preserving Jet Reference Frame

a. Jet frame coordinates for each grid point

To obtain time averages of a quantity in the jet reference frame, it is necessary to assign each point in the model grid a set of jet frame coordinates. Each grid point in the model already has a longitude ϕ and latitude Θ associated with it; thus, neglecting the depth coordinate (which is not affected by the jet frame coordinate transformation), the data at each point in time t can be described as located at the geographic coordinates (ϕ, Θ, t). In the jet reference frame that is used in this study, the geographic coordinates of each model grid point are transformed into the jet frame:

$$(\phi, \Theta, t) \rightarrow (\phi, d, t), \tag{A1}$$

so only one of the three coordinate values changes; longitude and time are retained. The new coordinate d is the distance between the grid point and the nearest point on the jet axis. Positive values of d are on the ''north'' side of the jet axis, and negative values are on the ''south'' side, with north (south) defined as to the left (right) of the direction of jet flow. (When the jet is sufficiently meandering, a point on the north side of the jet may actually be south of its nearest point on the jet axis, and vice versa.)

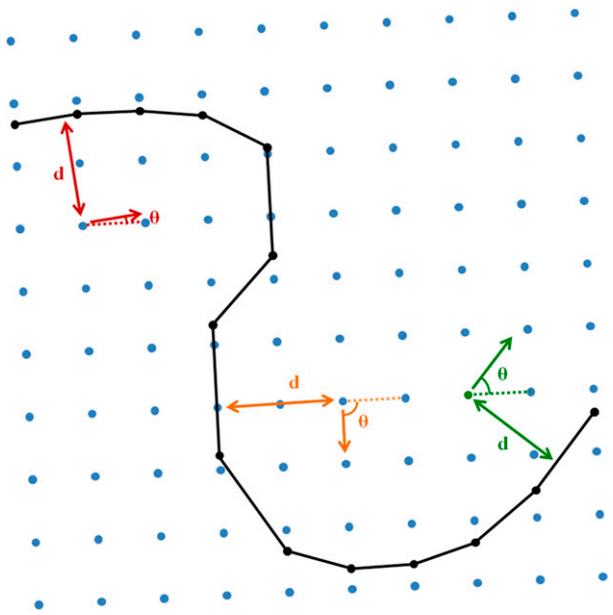

FIG. A1. Schematic illustrating how d and θ are computed for sample model grid points, relative to a defined jet axis (black line and dots).

The value of d is computed for each point as follows: Distances are first computed between discrete points on the jet axis and the array of grid points in the domain. Each grid point then has a discrete point on the jet axis that is the closest to it. The calculation of the distance is refined further by computing the orientation angle θ of the line segments between each discrete jet axis point. The value of θ is then determined for each model grid point by interpolating the values of θ from the two line segments adjacent to the nearest jet axis point. Finally, the exact value of d for the point is computed from the distance between the point and the perpendicular distance to the closest of the two line segments (Fig. A1). If the point that adjoins the two line segments (i.e., the original discrete jet axis point identified as closest) is closer than any other point on the two segments, then d is taken to be just the distance between the grid point and the original discrete jet axis point.

Note that for each model grid point and 5-day time period, the calculation just described yields a coordinate value d but also an orientation angle θ. The orientation angle of each point is important in the calculation of

vector mean quantities in the jet frame (e.g., velocities and fluxes), and therefore it is also necessary for the jet frame mean-eddy decomposition (appendix, section b).

b. *The jet frame mean-eddy decomposition*

Binning and averaging scalar quantities in the jet reference frame allows for a more faithful representation of the jet's synoptic structure in long-term time averages (e.g., Fig. 2). However, in order to use the jet frame's advantages to quantify the contribution of eddies to the mean circulation, it is necessary to define jet frame means of vector quantities (viz., velocities). Then the eddy part of the circulation can be defined as the deviation of the flow field at each time coordinate (i.e., 5-day time period) from the jet frame mean circulation.

Vector quantities that are binned and averaged in the jet frame must first be rotated by the local orientation angle θ so that the u axis is parallel to the jet orientation at the nearest point on the jet axis, that is,

$$\mathbf{u}_j \equiv \mathbf{R} \times \mathbf{u}, \tag{A2}$$

where $\mathbf{u} = (u, v)$, and $\mathbf{R}$ is the rotation matrix

$$\mathbf{R} = \begin{bmatrix} \cos\theta & \sin\theta \\ -\sin\theta & \cos\theta \end{bmatrix}. \tag{A3}$$

The resulting along-stream and cross-stream components of velocity $\mathbf{u}_j = (u_j, v_j)$ are then binned and averaged in the jet frame, in the same way scalar quantities are. This produces jet frame time means of along-stream and cross-stream velocity $\overline{\langle \mathbf{u}_j \rangle}^j = (\overline{\langle u_j \rangle}^j, \overline{\langle v_j \rangle}^j)$. To use these computed mean velocities to define the jet frame eddy velocity for each model grid point and 5-day time period, these mean velocities are then rotated back into the native model grid, using the inverse of the rotation matrix $\mathbf{R}^{-1}$ specific to that grid point and time,

$$\overline{\langle \mathbf{u} \rangle}^j \equiv \mathbf{R}^{-1} \times \overline{\langle \mathbf{u}_j \rangle}^j, \tag{A4}$$

and the jet frame eddy velocity is the difference between the jet frame mean in the Eulerian grid $\overline{\langle \mathbf{u} \rangle}^j$ and the total velocity, as defined in (9).

REFERENCES

Adamec, D., 1998: Modulation of the seasonal signal of the Kuroshio Extension during 1994 from satellite data. *J. Geophys. Res.,* **103,** 10 209–10 222, doi:10.1029/98JC00456.

Andrews, D. G., and M. E. McIntyre, 1976: Planetary waves in horizontal and vertical shear: The generalized Eliassen–Palm relation and the mean zonal acceleration. *J. Atmos. Sci.,* **33,** 2031–2048, doi:10.1175/1520-0469(1976)033<2031:PWIHAV>2.0.CO;2.

Bell, M. J., 1999: Vortex stretching and bottom torques in the Bryan-Cox ocean circulation model. *J. Geophys. Res.,* **104,** 23 545–23 563, doi:10.1029/1999JC900064.

Bingham, F. M., 1992: Formation and spreading of subtropical mode water in the North Pacific. *J. Geophys. Res.,* **97,** 11 177–11 189, doi:10.1029/92JC01001.

Bishop, S. P., 2013: Divergent eddy heat fluxes in the Kuroshio Extension at 144°–148°E. Part II: Spatiotemporal variability. *J. Phys. Oceanogr.,* **43,** 2416–2431, doi:10.1175/JPO-D-13-061.1.

——, and F. O. Bryan, 2013: A comparison of mesoscale eddy heat fluxes from observations and a high-resolution ocean model simulation of the Kuroshio Extension. *J. Phys. Oceanogr.,* **43,** 2563–2570, doi:10.1175/JPO-D-13-0150.1.

——, D. R. Watts, and K. A. Donohue, 2013: Divergent eddy heat fluxes in the Kuroshio Extension at 144°–148°E. Part I: Mean structure. *J. Phys. Oceanogr.,* **43,** 1533–1550, doi:10.1175/JPO-D-12-0221.1.

Bower, A. S., 1989: Potential vorticity balances and horizontal divergence along particle trajectories in Gulf Stream meanders east of Cape Hatteras. *J. Phys. Oceanogr.,* **19,** 1669–1681, doi:10.1175/1520-0485(1989)019<1669:PVBAHD>2.0.CO;2.

——, and H. T. Rossby, 1989: Evidence of cross-frontal exchange processes in the Gulf Stream based on isopycnal RAFOS float data. *J. Phys. Oceanogr.,* **19,** 1177–1190, doi:10.1175/1520-0485(1989)019<1177:EOCFEP>2.0.CO;2.

Charney, J. G., and M. E. Stern, 1962: On the stability of internal baroclinic jets in a rotating atmosphere. *J. Atmos. Sci.,* **19,** 159–172, doi:10.1175/1520-0469(1962)019<0159:OTSOIB>2.0.CO;2.

Chen, R., J. L. McClean, S. T. Gille, and A. Griesel, 2014: Isopycnal eddy diffusivities and critical layers in the Kuroshio Extension from an eddying ocean model. *J. Phys. Oceanogr.,* **44,** 2191–2211, doi:10.1175/JPO-D-13-0258.1.

Donohue, K., and Coauthors, 2008: Program studies of the Kuroshio Extension. *Eos, Trans. Amer. Geophys. Union,* **89,** 161–162, doi:10.1029/2008EO170002.

Emery, W. J., and R. E. Thomson, 2001: *Data Analysis Methods in Physical Oceanography.* Elsevier, 638 pp.

Gill, A. E., J. S. A. Green, and A. J. Simmons, 1974: Energy partition in the large-scale ocean circulation and the production of mid-ocean eddies. *Deep-Sea Res. Oceanogr. Abstr.,* **21,** 499–528, doi:10.1016/0011-7471(74)90010-2.

Greatbatch, R. J., X. Zhai, M. Claus, L. Czeschel, and W. Rath, 2010: Transport driven by eddy momentum fluxes in the Gulf Stream Extension region. *Geophys. Res. Lett.,* **37,** L24401, doi:10.1029/2010GL045473.

Greene, A. D., D. R. Watts, G. G. Sutyrin, and H. Sasaki, 2012: Evidence of vertical coupling between the Kuroshio Extension and topographically controlled deep eddies. *J. Mar. Res.,* **70,** 719–747, doi:10.1357/002224012806290723.

Hall, M. M., 1991: Energetics of the Kuroshio Extension at 35°N, 152°E. *J. Phys. Oceanogr.,* **21,** 958–975, doi:10.1175/1520-0485(1991)021<0958:EOTKEA>2.0.CO;2.

Hogg, N. G., 1994: Observations of Gulf Stream meander-induced disturbances. *J. Phys. Oceanogr.,* **24,** 2534–2545, doi:10.1175/1520-0485(1994)024<2534:OOGSMI>2.0.CO;2.

Holland, W. R., and P. B. Rhines, 1980: An example of eddy-induced ocean circulation. *J. Phys. Oceanogr.,* **10,** 1010–1031, doi:10.1175/1520-0485(1980)010<1010:AEOEIO>2.0.CO;2.

Howard, L. N., and P. G. Drazin, 1964: On instability of parallel flow of inviscid fluid in a rotating system with variable Coriolis parameter. *J. Math. Phys.,* **43,** 83–99.

Howe, P. J., K. A. Donohue, and D. R. Watts, 2009: Stream-coordinate structure and variability of the Kuroshio Extension. *Deep-Sea Res. I,* **56,** 1093–1116, doi:10.1016/j.dsr.2009.03.007.

Jayne, S. R., N. G. Hogg, and P. Malanotte-Rizzoli, 1996: Recirculation gyres forced by a beta-plane jet. *J. Phys. Oceanogr.,* **26,** 492–504, doi:10.1175/1520-0485(1996)026<0492:RGFBAB>2.0.CO;2.

——, and Coauthors, 2009: The Kuroshio Extension and its recirculation gyres. *Deep-Sea Res. I,* **56,** 2088–2099, doi:10.1016/j.dsr.2009.08.006.

Kelly, K. A., L. Thompson, W. Cheng, and E. J. Metzger, 2007: Evaluation of HYCOM in the Kuroshio Extension region using new metrics. *J. Geophys. Res.,* **112,** C01004, doi:10.1029/2006JE002678.

Kuo, H.-L., 1949: Dynamic instability of two-dimensional nondivergent flow in a barotropic atmosphere. *J. Meteor.,* **6,** 105–122, doi:10.1175/1520-0469(1949)006<0105:DIOTDN>2.0.CO;2.

Large, W. G., and S. G. Yeager, 2004: Diurnal and decadal global forcing for ocean and sea-ice models: The data sets and flux climatologies. NCAR Tech. Note NCAR/TN-460+STR, 105 pp.

——, and ——, 2009: The climatology of an interannually-varying air–sea flux data set. *Climate Dyn.,* **33,** 341–364, doi:10.1007/s00382-008-0441-3.

——, J. C. McWilliams, and S. C. Doney, 1994: Oceanic vertical mixing: A review and a model with nonlocal boundary layer parameterization. *Rev. Geophys.,* **32,** 363–403, doi:10.1029/94RG01872.

Maltrud, M. E., R. D. Smith, A. J. Semtner, and A. J. Malone, 1998: Global eddy-resolving ocean simulations driven by 1985–1995 atmospheric winds. *J. Geophys. Res.,* **103,** 30 825–30 853, doi:10.1029/1998JC900013.

——, F. O. Bryan, and S. Peacock, 2010: Boundary impulse response functions in a century-long eddying global ocean simulation. *Environ. Fluid Mech.,* **10,** 275–295, doi:10.1007/s10652-009-9154-3.

Meinen, C. S., and D. S. Luther, 2003: Comparison of methods of estimating mean synoptic current structure in "stream coordinates" reference frames with an example from the Antarctic Circumpolar Current. *Deep-Sea Res. I,* **50,** 201–220, doi:10.1016/S0967-0637(02)00168-1.

Mizuno, K., and W. B. White, 1983: Annual and interannual variability in the Kuroshio Current System. *J. Phys. Oceanogr.,* **13,** 1847–1867, doi:10.1175/1520-0485(1983)013<1847:AAIVIT>2.0.CO;2.

Mizuta, G., 2009: Rossby wave radiation from an eastward jet and its recirculations. *J. Mar. Res.,* **67,** 185–212, doi:10.1357/002224009789051227.

Niiler, P. P., N. A. Maximenko, G. G. Panteleev, T. Yamagata, and D. B. Olson, 2003: Near-surface dynamical structure of the Kuroshio Extension. *J. Geophys. Res.,* **108,** 3193, doi:10.1029/2002JC001461.

Pratt, L. J., J. Earles, P. Cornillon, and J.-F. Cayula, 1991: The nonlinear behavior of varicose disturbances in a simple model of the Gulf Stream. *Deep-Sea Res.,* **38,** S591–S622, doi:10.1016/S0198-0149(12)80025-2.

Qiu, B., and S. Chen, 2005: Eddy-induced heat transport in the subtropical North Pacific from Argo, TMI, and altimetry measurements. *J. Phys. Oceanogr.,* **35,** 458–473, doi:10.1175/JPO2696.1.

——, and ——, 2010: Eddy-mean flow interaction in the decadally modulating Kuroshio Extension System. *Deep-Sea Res. II,* **57,** 1098–1110, doi:10.1016/j.dsr2.2008.11.036.

——, ——, P. Hacker, N. G. Hogg, S. R. Jayne, and H. Sasaki, 2008: The Kuroshio Extension northern recirculation gyre: Profiling float measurements and forcing mechanism. *J. Phys. Oceanogr.,* **38,** 1764–1779, doi:10.1175/2008JPO3921.1.

Samelson, R. M., and J. Pedlosky, 1990: Local baroclinic instability of flow over variable topography. *J. Fluid Mech.,* **221,** 411–436, doi:10.1017/S0022112090003615.

Shay, T. J., J. M. Bane, D. R. Watts, and K. L. Tracey, 1995: Gulf Stream flow field and events near 68°W. *J. Geophys. Res.,* **100,** 22 565–22 589, doi:10.1029/95JC02685.

Smith, R., and P. Gent, 2002: Reference manual for the Parallel Ocean Program (POP). LANL/NCAR Tech. Rep. LAUR-02-2484, 73 pp.

——, and Coauthors, 2010: The Parallel Ocean Program (POP) reference manual. LANL/NCAR Tech. Rep. LAUR-10-01853, 140 pp.

Taguchi, B., B. Qiu, M. Nonaka, H. Sasaki, S.-P. Xie, and N. Schneider, 2010: Decadal variability of the Kuroshio Extension: Mesoscale eddies and recirculations. *Ocean Dyn.,* **60,** 673–691, doi:10.1007/s10236-010-0295-1.

Talley, L. D., 1983a: Radiating barotropic instability. *J. Phys. Oceanogr.,* **13,** 972–987, doi:10.1175/1520-0485(1983)013<0972:RBI>2.0.CO;2.

——, 1983b: Radiating instabilities of thin baroclinic jets. *J. Phys. Oceanogr.,* **13,** 2161–2181, doi:10.1175/1520-0485(1983)013<2161:RIOTBJ>2.0.CO;2.

Thomas, L. N., and T. M. Joyce, 2010: Subduction on the northern and southern flanks of the Gulf Stream. *J. Phys. Oceanogr.,* **40,** 429–438, doi:10.1175/2009JPO4187.1.

Tracey, K. L., D. R. Watts, K. A. Donohue, and H. Ichikawa, 2012: Propagation of Kuroshio Extension meanders between 143°E and 149°E. *J. Phys. Oceanogr.,* **42,** 581–601, doi:10.1175/JPO-D-11-0138.1.

Waterman, S. N., and S. R. Jayne, 2011: Eddy-mean flow interaction in the along-stream development of a western boundary current jet: An idealized model study. *J. Phys. Oceanogr.,* **41,** 682–707, doi:10.1175/2010JPO4477.1.

——, and B. J. Hoskins, 2013: Eddy shape, orientation, propagation, and mean flow feedback in western boundary current jets. *J. Phys. Oceanogr.,* **43,** 1666–1690, doi:10.1175/JPO-D-12-0152.1.

——, N. G. Hogg, and S. R. Jayne, 2011: Eddy–mean flow interaction in the Kuroshio Extension region. *J. Phys. Oceanogr.,* **41,** 1182–1208, doi:10.1175/2010JPO4564.1.

White, W. B., and J. P. McCreary, 1976: On the formation of the Kuroshio meander and its relationship to the large-scale ocean circulation. *Deep-Sea Res. Oceanogr. Abstr.,* **23,** 33–47, doi:10.1016/0011-7471(76)90806-8.

Wunsch, C., 1999: Where do ocean eddy heat fluxes matter? *J. Geophys. Res.,* **104,** 13 235–13 249, doi:10.1029/1999JC900062.

Yeager, S. G., 2013: Understanding and predicting changes in North Atlantic sea surface temperature. Ph.D. thesis, University of Colorado, 202 pp.

Young, W. R., 2012: An exact thickness-weighted average formulation of the Boussinesq equations. *J. Phys. Oceanogr.,* **42,** 692–707, doi:10.1175/JPO-D-11-0102.1.